Advanced Reactor Safeguards & Security

Imaging Techniques for Pebble Accountancy in Pebble Bed Reactors

Prepared for

US Department of Energy

Claudio Gariazzo[1], Sunil S. Chirayath[2], Thomas W. Elmer II[1], Sasan Bakhtiari[1], Dick Koehl[1], Mohammad Naraghi[2]

[1]Argonne National Laboratory

[2]Texas A&M University

January 2024

ANL/SS-24/1

Imaging Techniques for Pebble Accountancy in Pebble Bed Reactors

Prepared by
Claudio Gariazzo
Strategic Security Sciences Division, Argonne National Laboratory

Thomas W. Elmer II
Sasan Bakhtiari
Dick Koehl
Nuclear Science and Engineering Division, Argonne National Laboratory

Sunil Chirayath
Mohammad Naraghi
Texas A&M University

January 2024
Prepared for the DOE/NE-5 Advanced Reactor Safeguards and Security

1 Introduction

Researchers at Argonne National Laboratory (ANL) and Texas A&M University (TAMU) studied the ability of various dry-medium imaging systems to assist in identifying batches of pebbles (fuel, moderator, absorber) for pebble-fueled reactors – i.e., pebble bed reactors (PBRs). The concept arose as a complementary nuclear material control method for designers' use along with fuel burnup measurements for material accountancy needs. This study was a follow-on research from a developed wet-medium imaging system for identifying pebble artefacts. This originally proposed nuclear material control approach relied on identifying extrinsic non-radiological features embedded into the outer periphery of pebbles to account for various types of pebbles, where the wet-medium system relied on a coupling interface for scanned ultrasound images. When presented with the original concept, the PBR designers countered with an interest for dry-scanning techniques due to the volatility of reactor coolant.

We addressed the stated concern by investigating the utility of two dry-scanning systems for irradiated pebbles in PBRs: thermal imaging and eddy current inspection techniques. Moreover, PBR designers identified an additional need to not only monitor pebble tracking for nuclear material accounting and control (MC&A) needs but monitor integrity of the pebble for operational needs. Inroads made with one of the PBR designers, Kairos Power, allowed us to acquire numerous graphite-coated surrogate pebbles for use in experiments to support theoretical results. Working in concert, the teams at ANL and TAMU divided the tasks based on expertise and abilities in imaging techniques. ANL researchers examined eddy current inspection techniques while TAMU researchers focused their attention on the ability of thermal imaging. Both endeavors are included in sections 2 and 3 with a overall conclusion presented in section 4.

Overall, 2023 work consisted of a conceptual evaluation of eddy current and infrared scanning technologies to identify engineered features on the surface of the pure graphite pebbles supplied by Kairos and a series of experiments using both imaging techniques which could be used to eventually develop a dry pebble identification and integrity assessment method. Eddy current method utilized surface features (engineered or due to damage) to identify a pebble batch while thermal imaging capabilities were evaluated for identifying (subsurface) features (engineered or due to damage) within the outer layer of graphite (less than 5mm) using the inherent heat signature sourced from the pebble's interior.

2 Eddy Current Technology

Eddy Current (EC) inspection is a mature non-destructive examination (NDE) technology that is fast and economical. Minimizing ex-core time while sorting pebbles is ideal in PBR designs, however enough analytical data must be acquired for identifying batches of pebbles, if not individual pebbles. Based on various criteria including initial uranium enrichment and first date of introduction into the reactor, pebble batches can be identified by various engineered and/or created artefacts on the surface of the pebble. Newer batches of pebbles can be returned into circulation immediately with random samples pulled out for complete inspection while older batches can be separated out for more complete inspection or discharge entirely. EC probes can be adapted for a broad range of in-situ inspection applications and ANL has extensive experience with the design and development of advanced EC probes, both hardware [1] and software [2]. While EC probes for NDE applications typically operate below 200°C, development is being pursued by the industry to increase the operating temperatures of these probes to 600°C within 2024 [3], and probes are reported in the literature to over 800°C [4]. Both of which are characteristic of internal temperatures found within a PBR.

2.1 Eddy Current background

The basic principle of Eddy Current testing (ECT) is illustrated in Figure 1. An alternating current in the coil induces eddy currents in the conducting material to be inspected, which in turn creates a secondary field that is picked up by the coil. Physical interruptions, such as defects in the material, cause changes in the received signal, which can be interpreted by the operator. EC probes can be designed for optimal sensing of specific features in the material under test. A hypothetical EC sensor is illustrated in Figure 2, wherein a graphite-coated pebble rolls though an array of coils, which collect data in real time. Such a sensor would be able to detect flaws, impregnations, or manufactured grooves in the outer layer of the pebble.

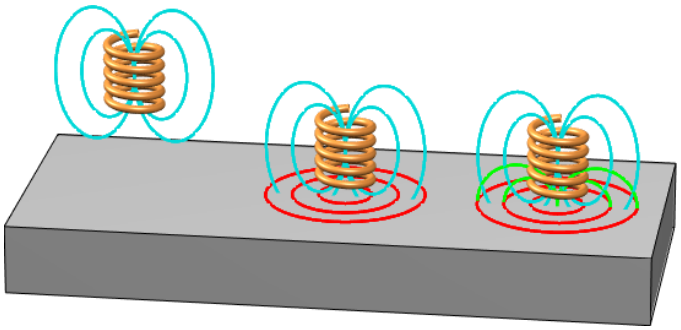

Figure 1. Explanatory diagram of Eddy Current testing.

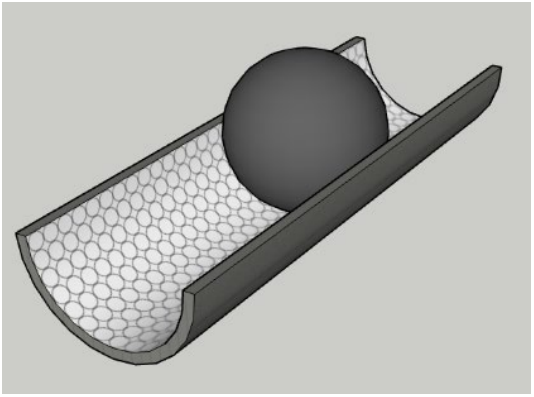

Figure 2. Hypothetical Eddy Current array sensor for inspecting graphite spheres

The Beer-Lambert law relates the attenuation of a plane electromagnetic wave to the properties of the material through which the wave is travelling. In a material in which the attenuation coefficient, α, does not vary, the law can be expressed as Equation (1), where $I(z)$ is the intensity of radiation at depth z, and I_0 is the intensity at the surface. The depth of penetration, δ_p, is defined as the depth at which the intensity decays to 1/e of its surface value, i.e., where $z = 1/\alpha$. For EC techniques, the standard depth of penetration is given by Equation (2), where μ is the magnetic permeability, σ is the electrical conductivity, and f is the frequency of the electromagnetic wave.

$$I(z) = I_0 e^{-\alpha z} \quad (1)$$

$$\delta_p = \sqrt{\frac{2}{\omega\mu\sigma}} = \frac{1}{\sqrt{\pi f \mu\sigma}} \quad (2)$$

From this, one can see that the depth of penetration of an electromagnetic wave is dependent on the excitation frequency, the magnetic permeability, and electrical conductivity of the material. However, in practical use, we are not dealing with true plane waves impinging on infinite half-plane surfaces. For real-world applications, the size of the coil is also important [5]. As a general rule-of-thumb, the coil size should be approximately proportional to the depth of penetration desired. This could be a limiting factor for the resolution of array-type probes. Also, it should be reiterated that the standard depth of penetration represents that point where the intensity decays to 1/e of its surface value. The wave can still penetrate further than this, but the returned signal is weaker.

The electrical conductivity of graphite has a wide range of values, depending on factors such as: plane of incidence with respect to the plane of aligned graphite sheets [6], density of graphite [7], and temperature [8]. Based on data from reference [8], a plot of depth of penetration versus frequency is given in Figure 3. From this figure, we can see that frequencies less than 100 kHz should be able to penetrate 5mm into graphite. However, it should be noted that higher frequencies can also be used if the application calls for it, as properly designed EC probes can still sense discontinuities at multiple δ_p within the material.

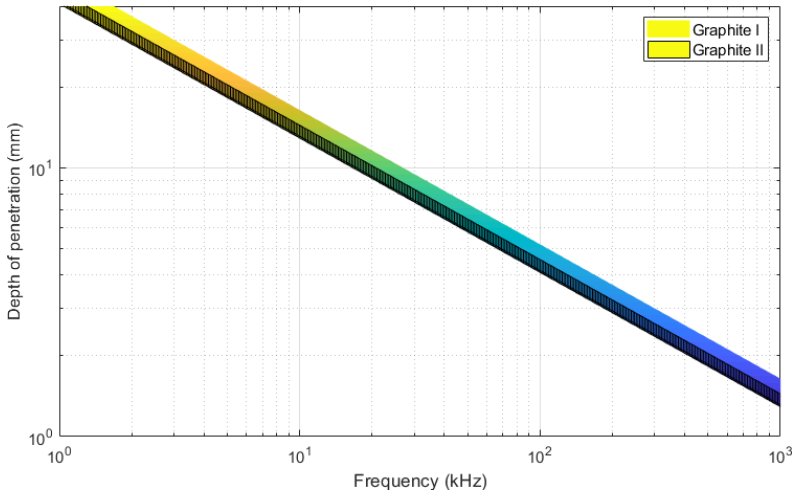

Figure 3. Plot of depth of penetration vs frequency based on Powell, et al. Thicknesses of the lines represent the surface plotted over the range from 0-1000° C.

2.2 Numerical Electromagnetic Modeling

The optimal frequency for investigating a sample is a complicated relationship due to many factors. Selection of the optimal test frequency is often a tradeoff between EC depth of penetration and sensitivity. While the Beer-Lambert law's depth-of-penetration calculation is a good first-order calculation for understanding the ability to interrogate the interior of an object, techniques such as ECT also depend on other factors, e.g., the ability to set up currents in the material. While lower frequencies can penetrate further, higher frequencies have higher current density and can more readily set up the required eddy currents in the material. In the extreme case, picture a vacuum, which has effectively infinite depth of penetration, but no signal return. On the other end, a perfect conductor will have great signal return, but all the currents are on the surface, and one would be unable to see anything beneath the skin of the conductor at very high frequencies. In order to select the proper frequency and coil size for testing pebble fuel samples, we performed simulations using a Volume Integral Method (VIM), as described in the following sections. From computational standpoint VIM is significantly less intensive than Finite Element Method (FEM), as the discretization is mainly confined to the discontinuities within the model geometry.

2.2.1 Effect of electrical conductivity

A wide range of electrical conductivities can be found in the literature for graphite. These can depend on factors such as the compactness of the graphite and the alignment of the graphite sheets. Due to the 2-dimensional nature of the constituent graphene, graphite is highly anisotropic in its physical properties. For

example, electrical conductivity is very high in the direction parallel with graphene layer planes. However, in the perpendicular direction electron transfer is minimal, resulting in low conductivity.

We performed simulations using two values of the conductivity found in the literature, $17x10^3$ S/m and $1x10^5$ S/m. Figure 4 shows impedance plots of the expected signal response from a subsurface air void (1 mm^3 volume at 4.5 mm deep) at various frequencies. Figure 4(a) shows that at the lower conductivity, the frequencies around 1000 kHz or higher would have better response than lower frequencies. However, for the higher conductivity in Figure 4(b), frequencies between 500 kHz and 1000 kHz would have better sensitivity to subsurface discontinuities.

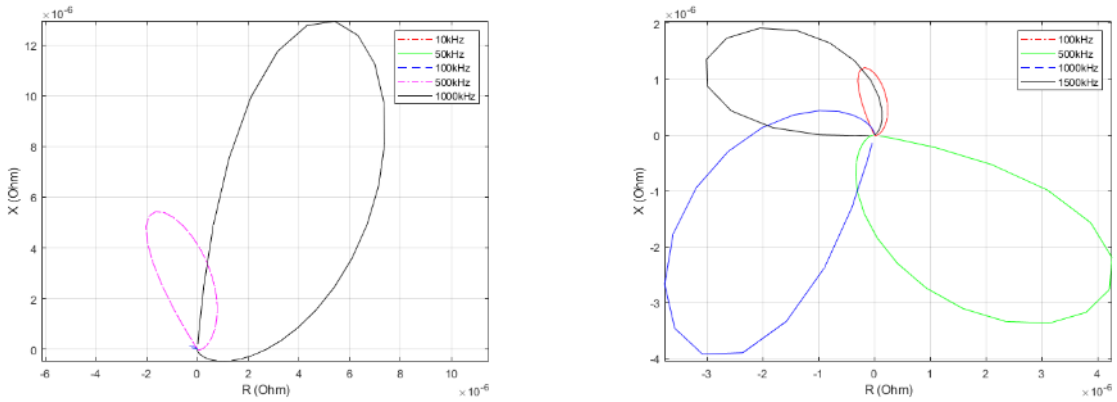

(a) (b)

Figure 4. Effect of conductivity on signal response. Shown here are simulations for a subsurface air void in graphite with conductivities of (a) $17x10^3$ S/m and (b) $1x10^5$ S/m.

Presented in the following sections are the results of simulations performed assuming a conductivity value for graphite of around $1x10^5$ S/m, as provided in Reference [8].

2.2.2 Effect of coil diameter

Another factor that can influence the probe response and plays into the spatial resolution is the diameter of the interrogating coil. While smaller coils can intrinsically be placed closer together in arrays, improving resolution, they may not be able to establish suitable eddy current density at the depths required. Figure 5 shows the calculated signal amplitude as a function of position using two different coil sizes for the same model geometry as Figure 4. The subsurface discontinuity is centered at a position of 20 mm. We can see that the 6 mm coil has an order of magnitude higher response than the 3 mm coil. However, if this is an acceptable loss, the 3 mm coil may be preferred for its higher resolution. Again, the simulation results indicate that at this conductivity, 500 kHz to 1000 kHz is a better range of test frequencies for the 6 mm coil.

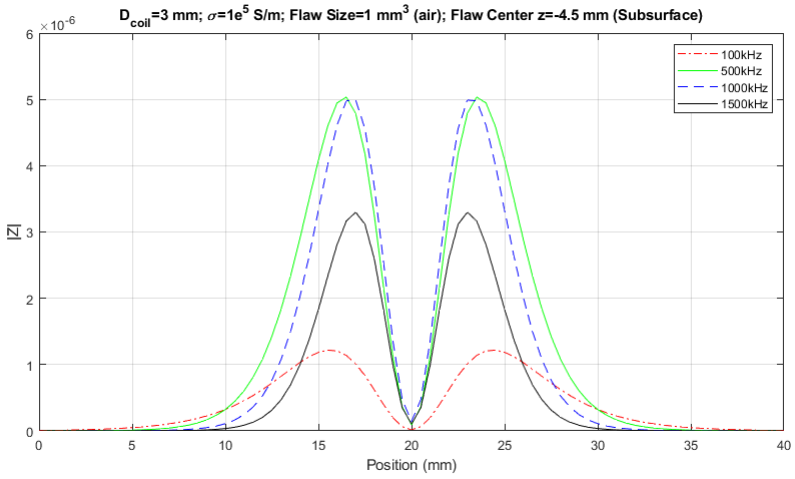

(a)

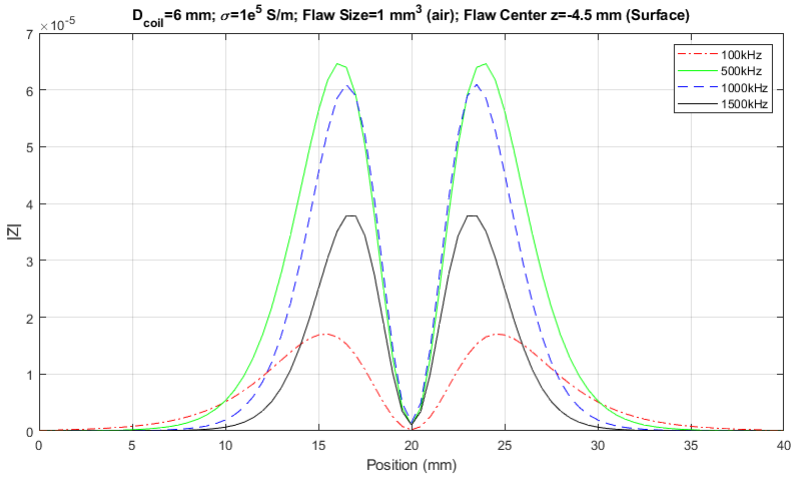

(b)

Figure 5. Comparison of amplitudes of signal response at two different coil diameters. Shown here are simulations using (a) a 3 mm coil and (b) a 6 mm coil.

2.2.3 Effect of flaw location

One of the capabilities of EC testing is the ability to determine depth by observing the phase and/or amplitude of the measured signal. Figure 6 shows the results of simulations of a 3 mm diameter coil interrogating 1 mm³ air voids centered near the surface at a depth of 0.5 mm, and near the layer interface at a depth of 4.5 mm. In comparing the figures, one can observe how depth-of-penetration affects the amplitude of the signal at various frequencies. While 1500 kHz produces a very strong response at the surface, it has more loss at greater depths than the lower frequencies. Likewise, one can also observe that the frequencies that penetrate deeper exhibit a larger phase shift caused by the flaw at the greater depth. For flaws/inclusions near the surface, one would then choose frequencies >1000 kHz for highest signal response. However, for detecting flaws at greater depths a frequency around 500 kHz is expected to produce a stronger signal.

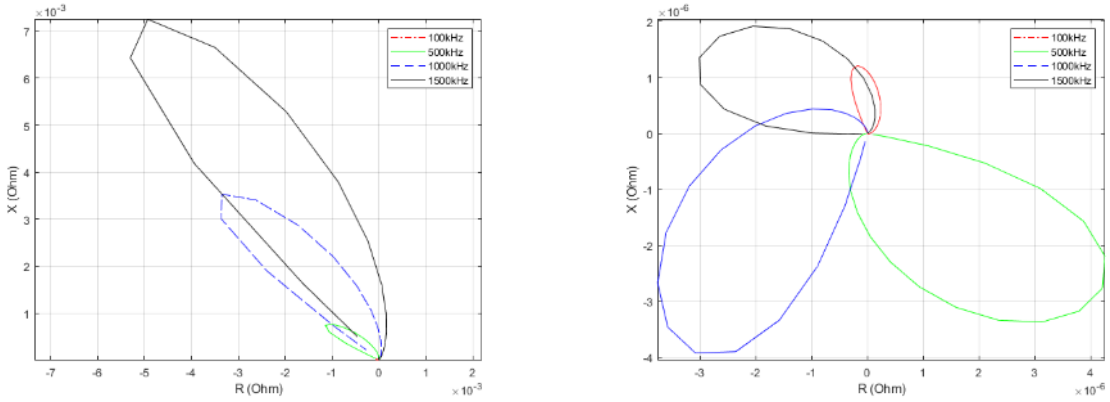

(a) (b)

Figure 6. Simulation of an air void at different depths. Shown are simulations centered at (a) 0.5mm, and (b) 4.5mm in depth.

2.3 Experimental work

The Sensors, Instrumentation, and Non-Destructive Evaluation (SINDE) group at Argonne has access to a variety of EC instruments and probes to test on the pebbles. The team performed initial tests using a handheld EC device, followed by a portable instrument, from Zetec Inc., designed for balance of plant use. Initial tests used pencil probes, which use a single coil for spot measurements. However, rapid inspection of whole pebbles requires the use of array probes that are composed of a large number of elements. Though we had an array probe from another project, the manufacturer, GE, no longer supports nor sells this item. The team attempted to find another source and researched alternatives with Zetec. As a note on the frequency response of the tape probe, the Zetec representative stated that while the GE probe runs best at frequencies over 1000 kHz, their tape probes have had good results at 300 kHz – 6000 kHz. We purchased a probe from Zetec, but we were unable to install it to operate simultaneously with the old probe in the time available. So, the EC array probe data presented in this report are all associated with the available thin-film flexible probes.

We initially had access to the 4 cm solid graphite pebble shown in Figure 7. We also borrowed a 6 cm pebble sample from another Argonne colleague, shown in Figure 8. This sample appears to be from Brown Boveri BBC/HRB. This pebble is a few years old and has been polished over the years. Later, we received ten additional 4 cm pebbles in Group 2: nine solid pebbles and one annular simulant pebble, discussed later in this report.

Figure 7. Initial 4 cm pebble.

Figure 8. 6 cm pebble on loan to SINDE group.

2.3.1 *Point measurements to estimate conductivity*

As noted previously, a wide range of electrical conductivities can be found in the literature for graphite. We performed simulations using two values of the conductivity found in the literature, 17×10^3 S/m and 1×10^5 S/m. Based on those simulations, it was decided we should target the 800 kHz - 1200 kHz range, with lower conductivities requiring higher frequencies.

Measurements on the 4 cm pebble using a hand-held EC Conductivity Probe were below its level of sensitivity, indicating the conductivity is on the lower end of values for graphite reported in the literature. We then made a series of measurements using an EC pencil probe to compare against materials of known conductivity in order to make a first-order approximation on conductivity.

One way to calibrate a probe's response, in the absence of a suitable calibration standard, is the probe response to lift-off, as illustrated in Figure 9. Lift-off is the difference between signal at the surface of the item under inspection and the signal in air, as the probe is lifted off the surface. The lift-off signal is rotated to 0° phase and normalized to a set amplitude. This restricts lift-off to the horizontal axis, so any signal with a vertical component can be viewed as flaw-like. However, this change in phase and amplitude due to lift-off varies with the conductivity of the material under examination. From this, one can in turn make an estimation of the conductivity of an unknown sample.

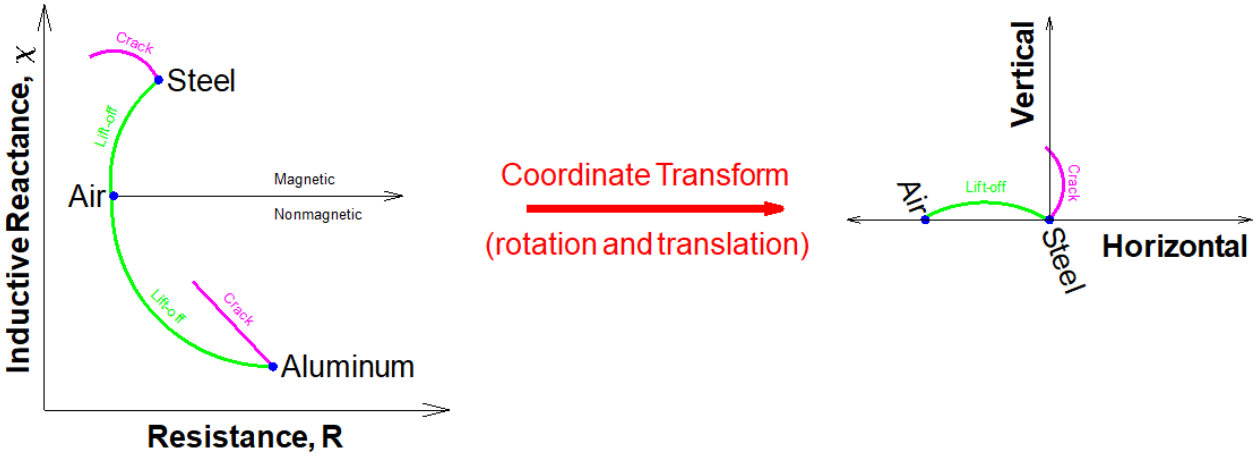

Figure 9. Illustration of lift-off calibration.

Data were collected on various conductivity calibration samples and compared to the lift-off on a pebble test piece. Figure 10 shows calibrated lift-off data collected at 1000 kHz on a copper calibration sample and the 4 cm graphite pebble. In the case of the pebble, the pencil probe is moved from air to the sample 5 times at each of the multiple measurement locations. One can observe that there is a slightly higher response in the final location group of the pebble. This likely indicates the presence of a subsurface feature at that location of the pebble, thus affecting the lift-off response.

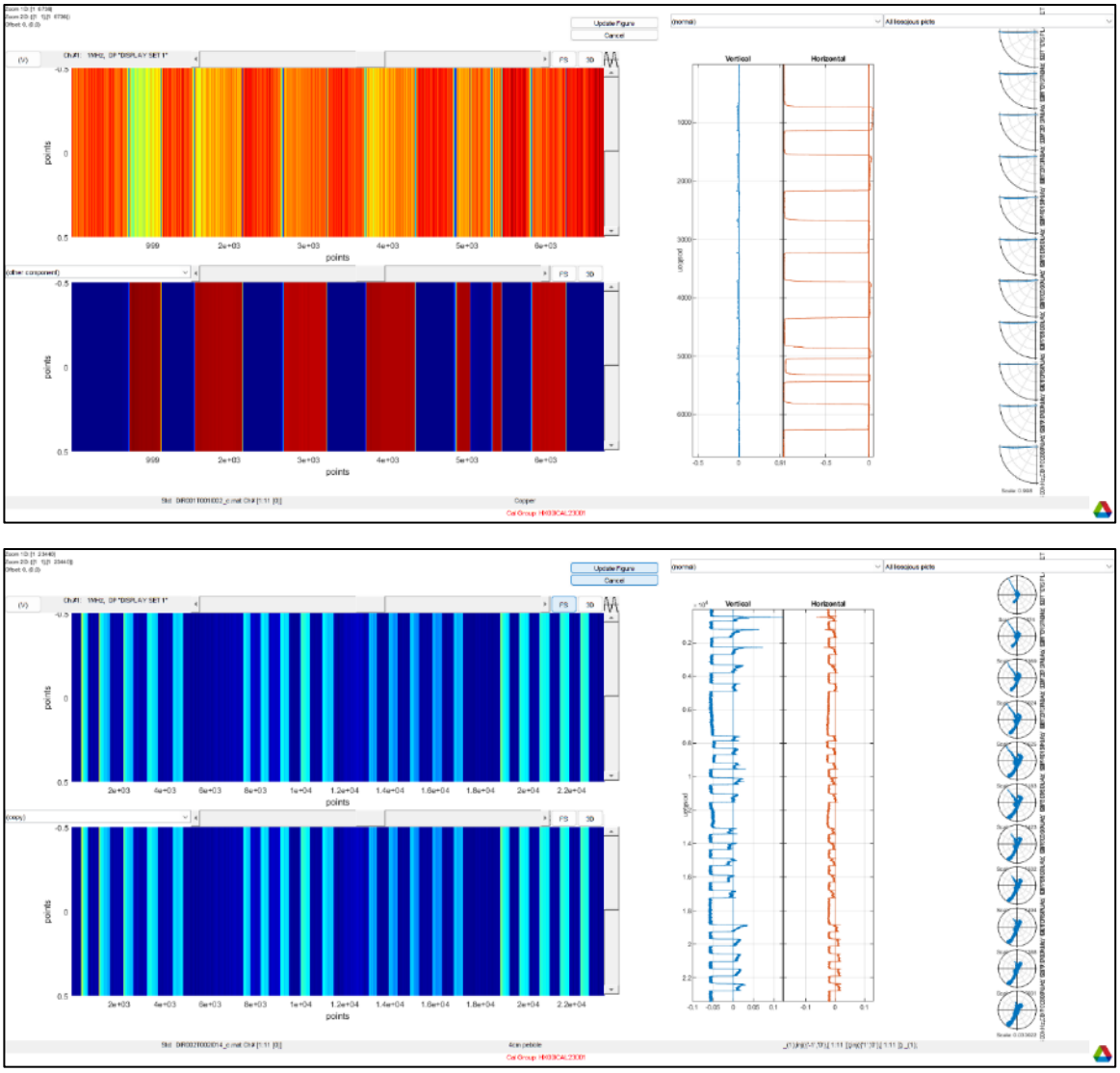

Figure 10. Eddy Current lift-off data on copper (top) and the 4 cm pebble (bottom) collected with a pencil probe.

Figure 11 shows the amplitude of the lift-off signal at 1000 kHz on various conductivity calibration standards and the two pebbles. It can be noted that in general the 6 cm pebble has a higher conductivity than the 4 cm pebble. Also displayed are Lissajous curves of the lift-off response showing the relative phase shift for the various materials. There is some color ambiguity in Figure 11 due to the large number of lines plotted, however, it is helpful to note that small amplitude lines are graphite pebble measurements, while large amplitude lines are other conductors. The large amplitude green line at about 220° is ferrous steel, which introduces magnetic complications. The low amplitude green line at 315° is the 6 cm pebble.

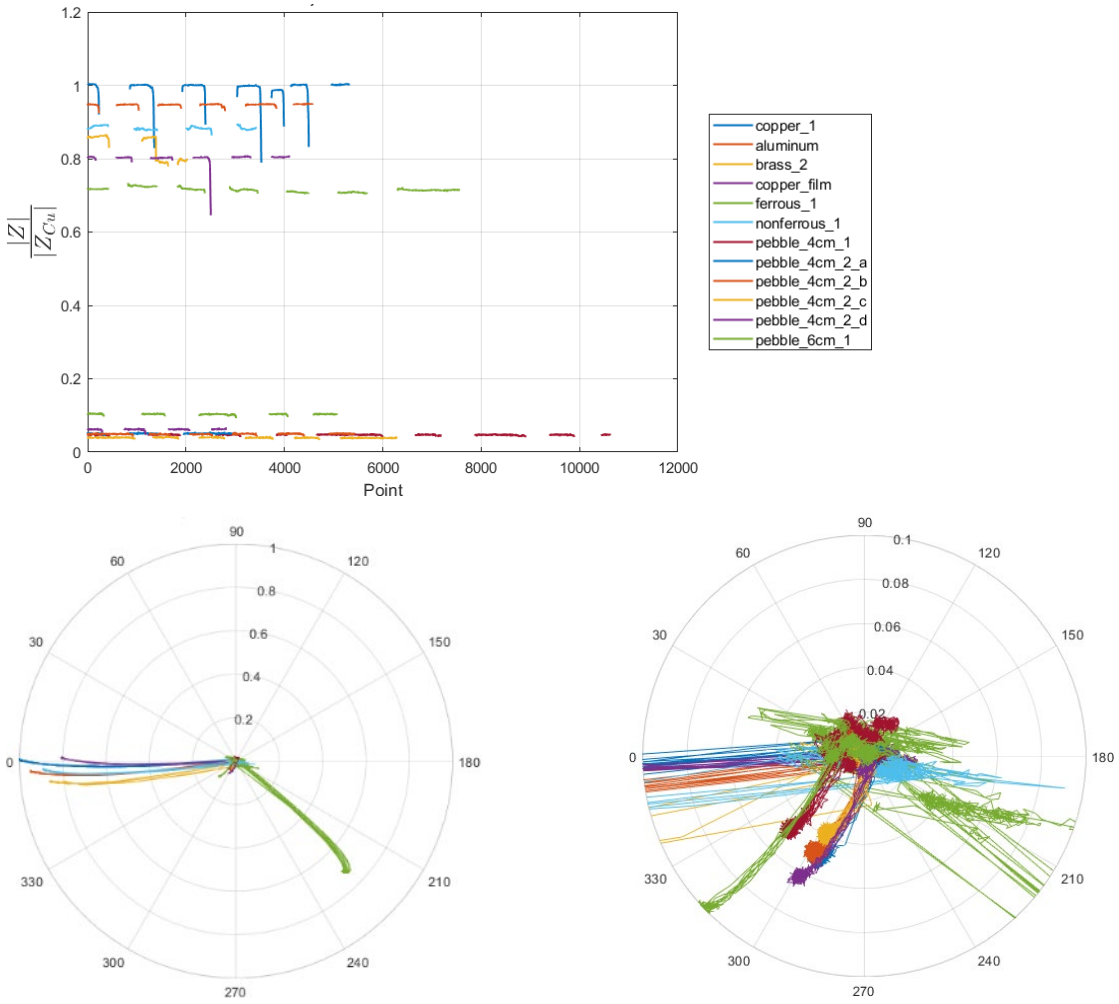

Figure 11. Comparison of calibrated signals collected on various samples at 1000 kHz. Shown are the lift-off amplitudes (top), Lissajous curves (bottom-left) and zoomed in to show graphite pebble responses (bottom-right).

Figure 12 shows simulations of lift-off amplitude response versus conductivity, normalized to the response of a good conductor, namely copper. The test frequency ranges from 600 kHz to 1200 kHz. The coil diameter used for these simulations is 3 mm. Overlaid on this plot are the calibrated measurements for lift-off from the 4 cm pebble, albeit using a coil with a slightly smaller diameter. The data in Figure 12 implies a conductivity well below the 10^5 S/m level reported in some references. Our simulation results indicate that frequencies in the 1000 kHz range are more appropriate for EC examination of graphite pebbles.

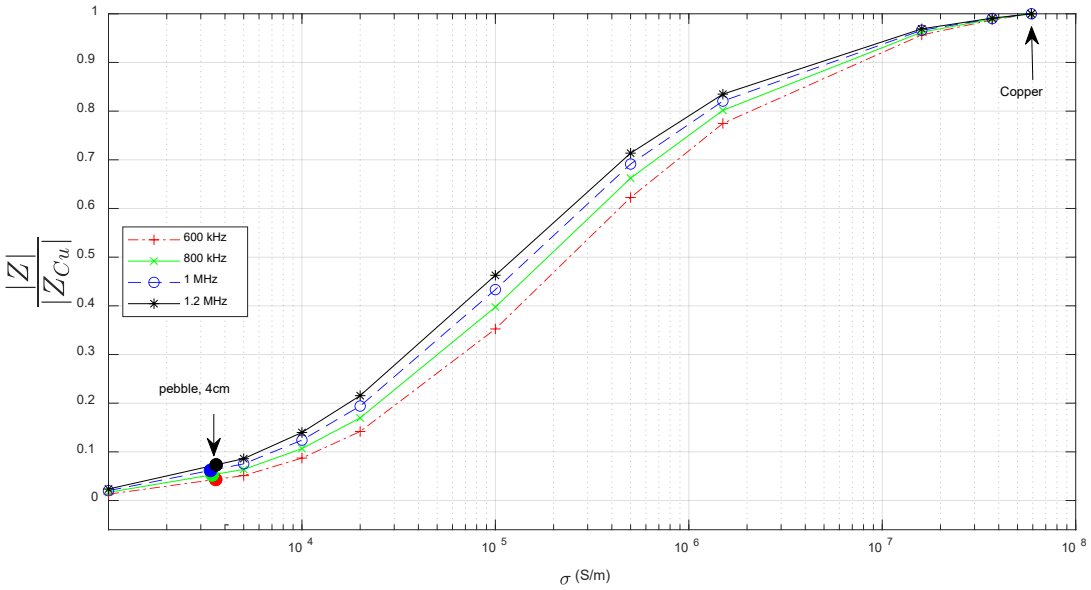

Figure 12. Simulations of lift-off amplitude response versus conductivity, normalized to the response of copper, for a 3mm coil. Included are simulations at multiple frequencies. Overlaid on this plot are the measured values for the 4 cm pebble, collected with a smaller diameter coil.

2.3.2 Pencil Probe scans

After acquiring fixed-point lift-off measurements as described above, the 4 cm sample was placed on a rotating motion control stage and horizontal scans were collected with the pencil probe, as shown in Figure 13. The probe elevation was adjusted, and its angle was rotated to make the coil reasonably parallel to the surface. Due to the complex nature of the positioning with probe rotation and limited availability of space for positioning hardware, these adjustments were performed manually. Once the probe was manually positioned, the rotating stage was activated as the data was acquired.

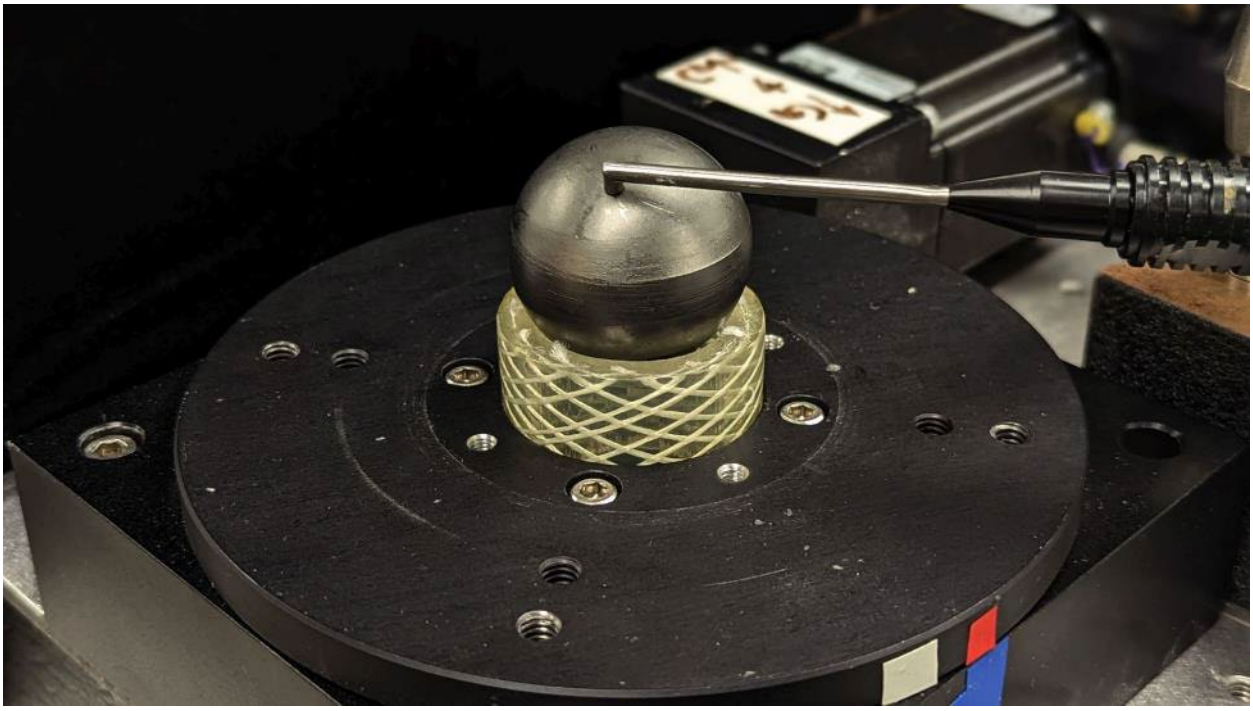

Figure 13. A 4 cm pebble being scanned with a pencil probe on a rotating motion control stage.

In the initial scan, a feature was detected at about 30° down from the top of the pebble. Later scans returned to the same region and the elevation was adjusted 5° down to locate the largest signal from the feature, which is shown in Figure 14. Multiple scans are provided, illustrating the reproducibility of the feature discovered at this elevation. The feature length and phase shift match upon repeated scans. The tight phase grouping of the probe response at different frequencies indicates that this is a feature just below the surface. Note that the amplitude of the probe response drops significantly from its peak value at 1200 kHz to the lowest test frequency of 500 kHz.

Another feature was detected in the lower hemisphere of the same pebble. While the location was reproducible, the phase and amplitude of the probe response were not. The initial view was that the vertical positioning was just on the edge of the feature and thus subject to edge effects. However, further manual adjustments to the position did not result in an improved signal.

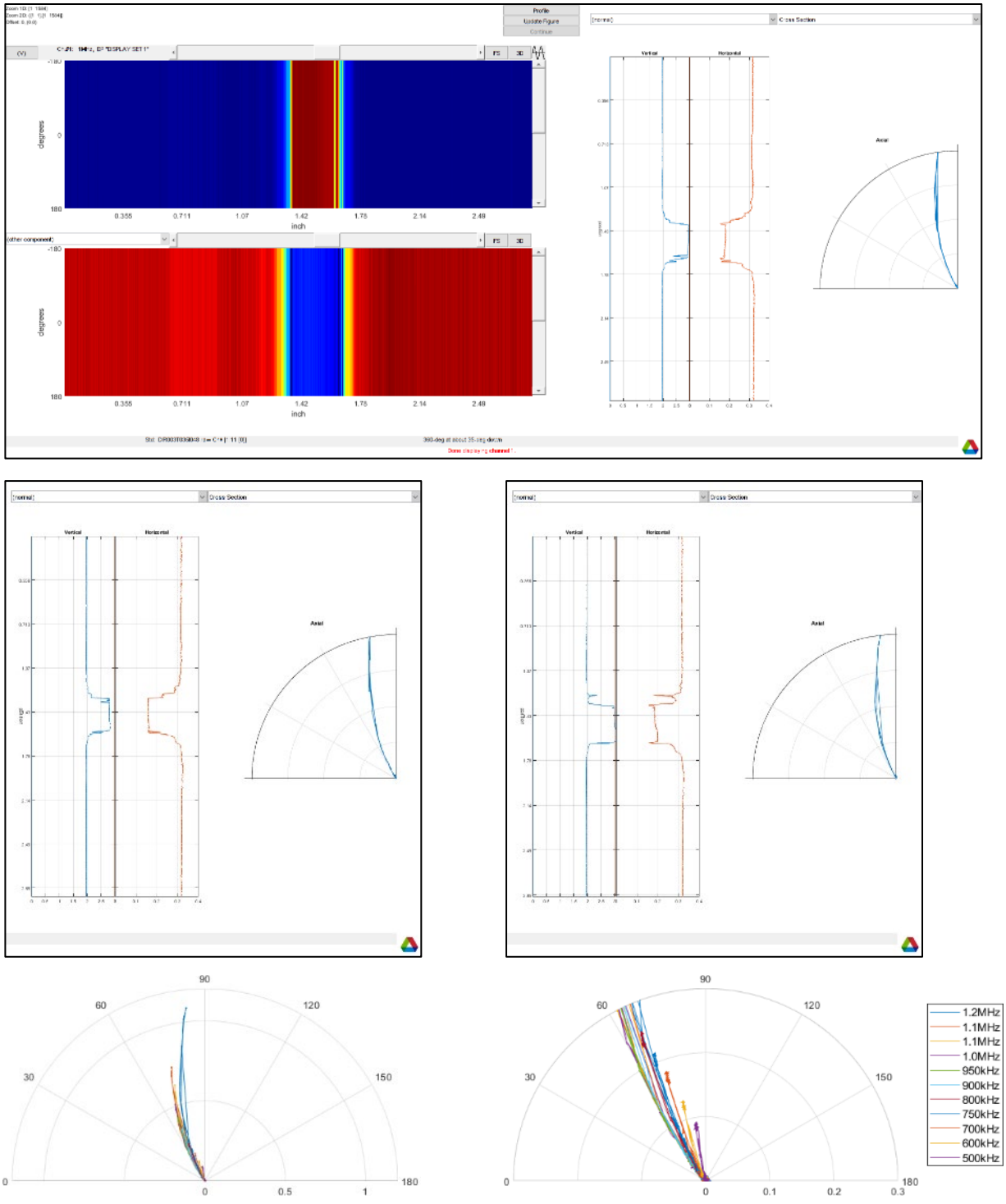

Figure 14. Data acquired on scans at about 35° down from the top of the pebble. Shown here are multiple scans, illustrating the reproducibility of the feature discovered at this elevation. Also shown are the probe responses at different frequencies (bottom).

Pencil probe scans were assembled to create a rough map of the pebble as shown in Figure 15. Displayed are amplitude maps at 1200 kHz and 500 kHz. As can be seen, the signal response decreases for the upper feature at the lower frequency, as expected for a low conductivity graphite material. However, the intensity of the lower feature does not decrease as much. One possible explanation is a change in conductivity due to a local coincidental alignment of graphene sheets in this area. However, the non-reproducibility of the lower feature makes it difficult to confirm the nature of the signal. A projection of this map onto a sphere is shown later in Figure 19.

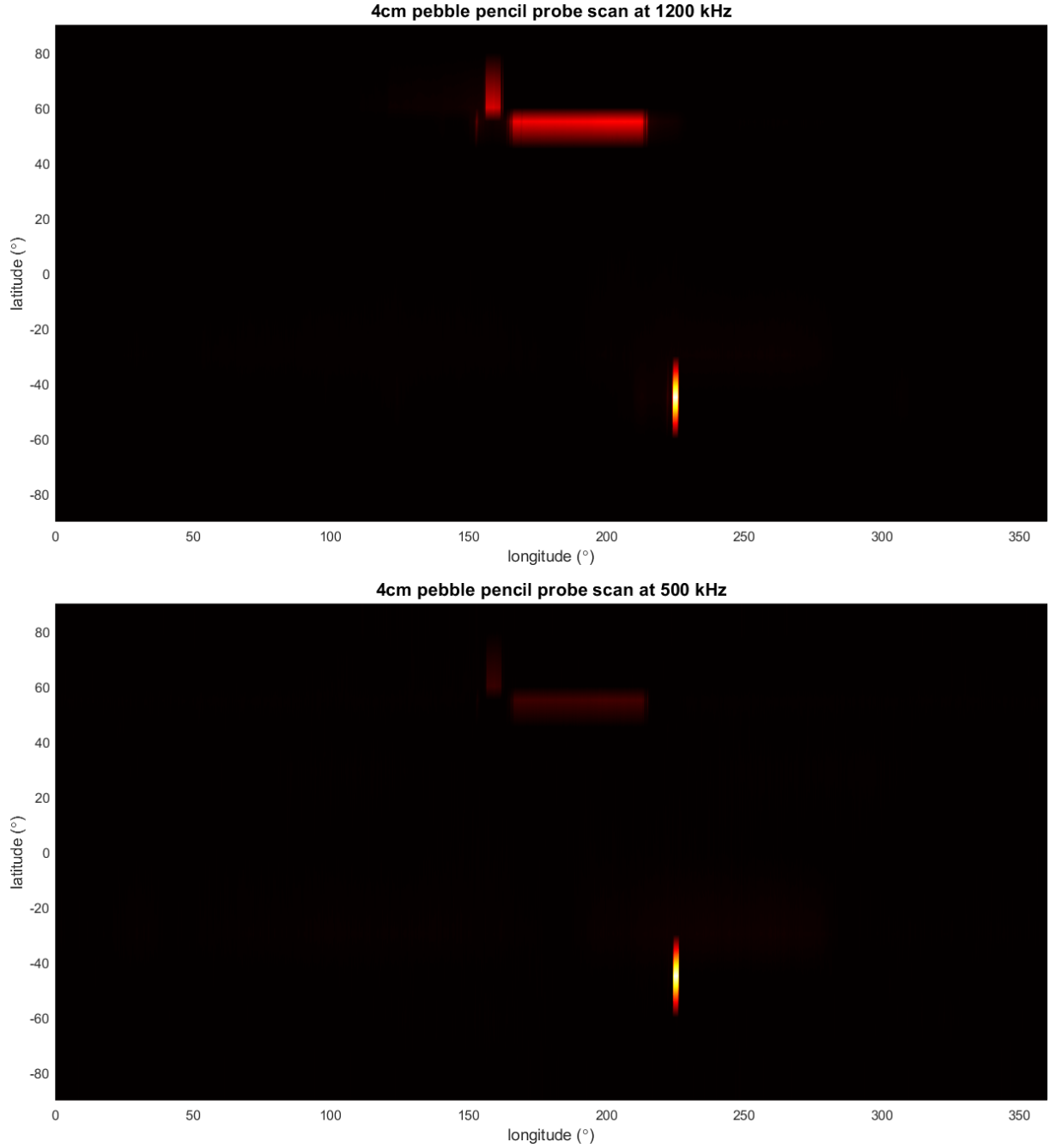

Figure 15. A rough map of the pebble using pencil probe scan amplitudes at 1200 kHz (top) and 500 kHz (bottom).

2.3.3 *Preliminary array probe results*

After the pencil probe scans, we collected preliminary data using a thin-film array probe. Initially, we manually held the array to conform to the surface of the pebble as the pebble was rotated, as illustrated in Figure 16. This method is prone to error. A 3D printed mount for the array probe was subsequently designed and tested, also shown in Figure 16. This mount was later used on Group 2 pebbles.

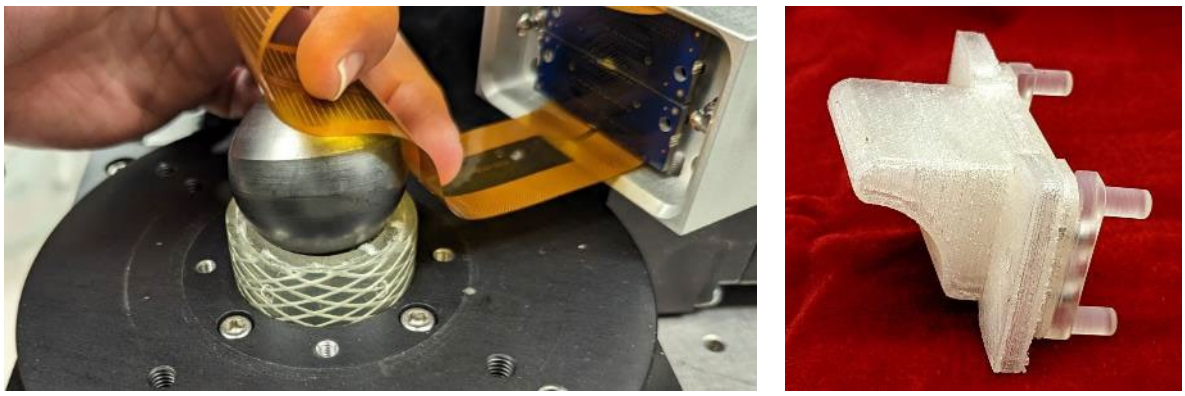

Figure 16. Photo demonstrating manual placement of thin-film array probe (left). A mount was designed to improve results (right).

One scan of the upper hemisphere of the pebble showed a feature at about the same location as the pencil probe scan, shown in Figure 17. Due to the highly variable nature of the hand-held scan, this result was not reproducible and therefore should be considered preliminary. A further note for interpreting this figure is that lower coils in the figure correspond to higher latitudes on the sphere, so the plot should be flipped for proper orientation.

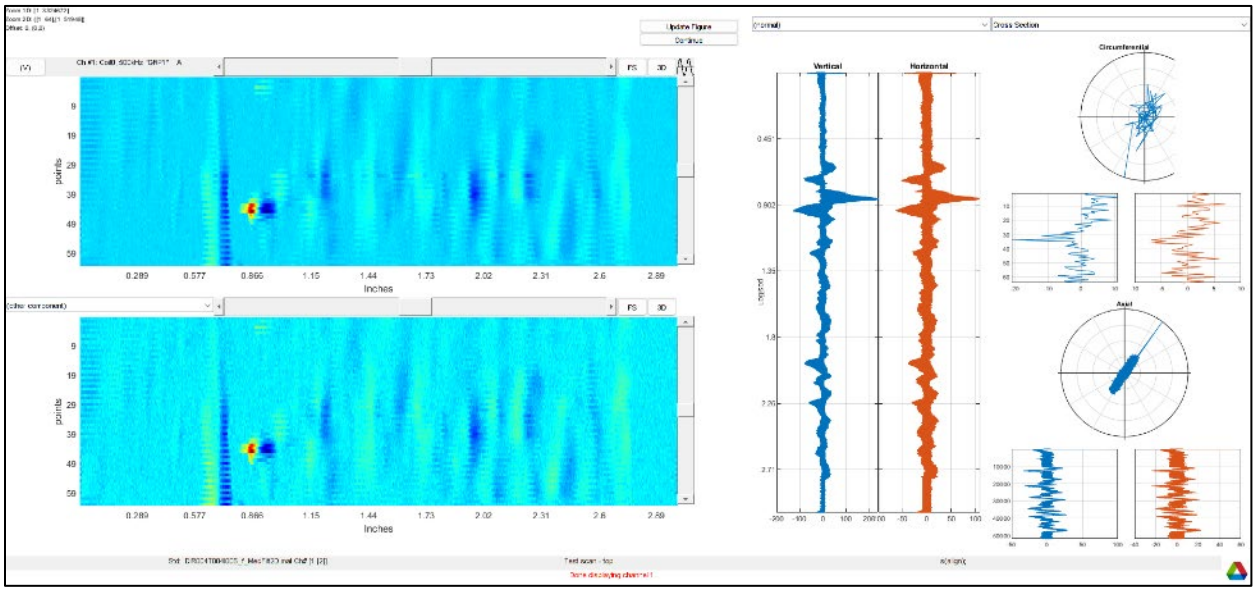

Figure 17. Array probe scan of the upper hemisphere of the pebble.

An amplitude map of the entire pebble after flipping the above data and joining it with the lower hemisphere data is shown in Figure 18. This data was acquired at 500 kHz and the results were not reproduced at other frequencies. The maps for both the pencil probe and array probe scans were projected onto spheres and can be compared in Figure 19. It should be noted that the necessary filtering of the array probe data could be shortening the apparent longitudinal length of longer features such as the one seen in the pencil probe scan.

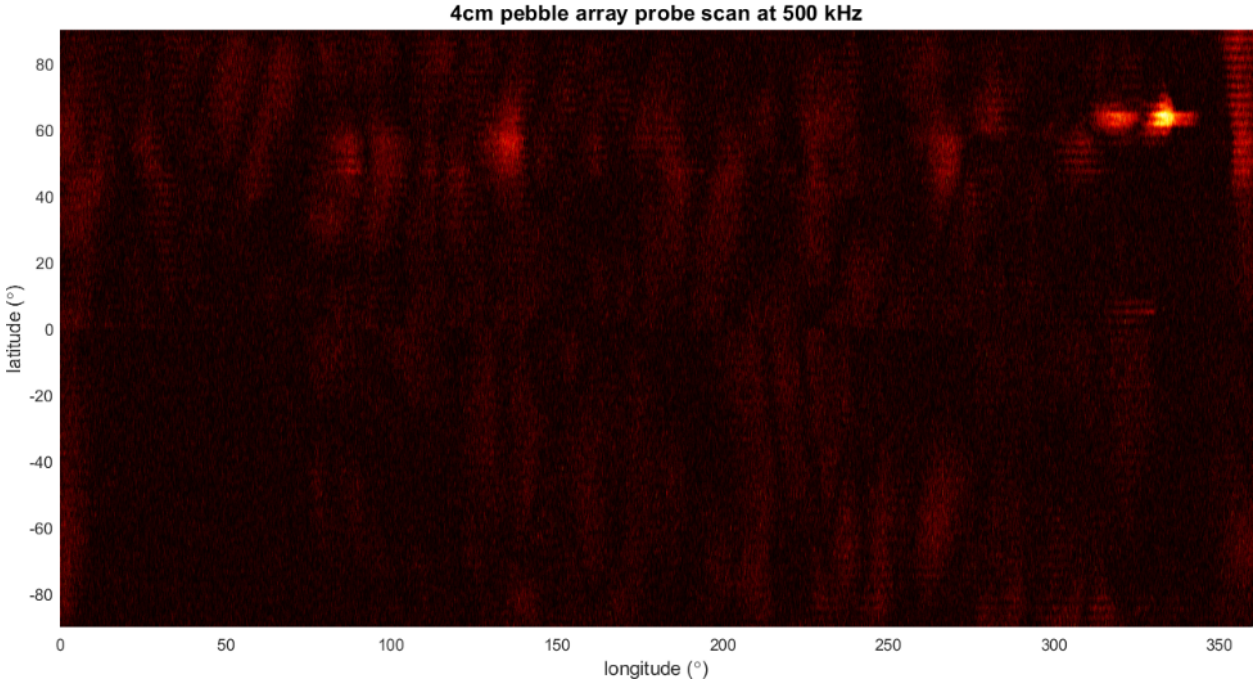

Figure 18. Map of the entire pebble using thin-film array probe amplitude at 500 kHz.

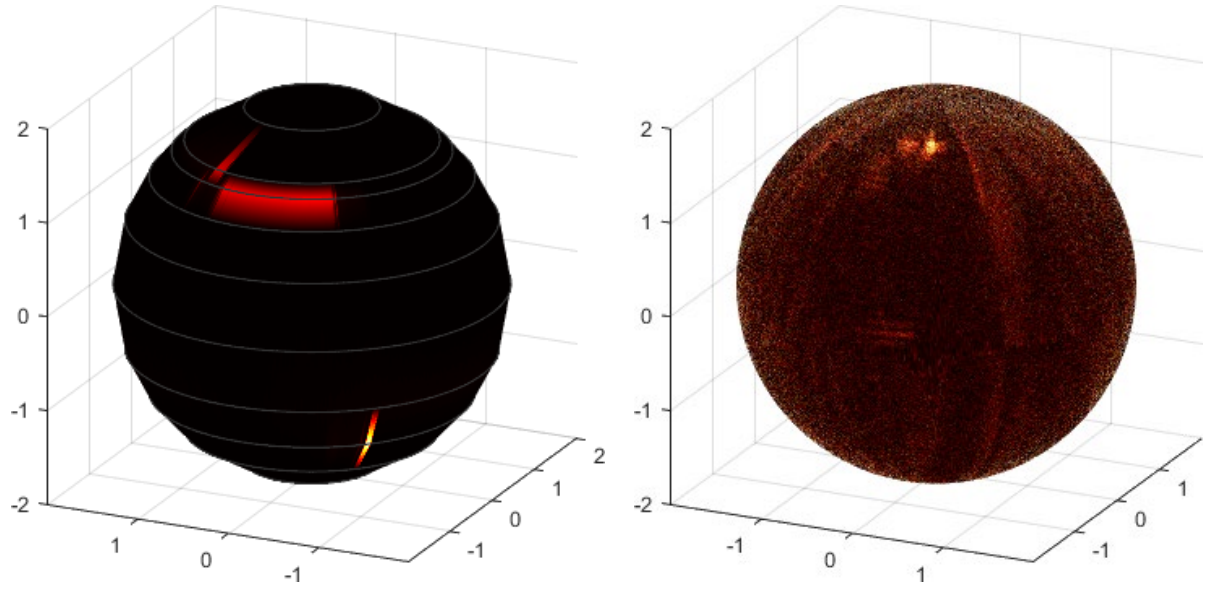

Figure 19. Projections of scans from the pencil probe (left) and array probe (right) for comparison.

Initial tests with the array probe were performed by manually holding the probe to the surface of the pebble as it rotated. We later created a probe holder that conformed to the pebble, using additive manufacturing. Circumferential scans were collected with a pencil probe at various latitudes on the 4 cm pebble. Based on these measurements, it was decided that a wound-coil flexible array probe would be needed to get better current flux density in the pebbles.

2.3.4 Group 2 pebbles

A second group of pebbles was received for EC inspection, shown with the original pebbles in Figure 20. The majority of pebbles in this batch consisted of nine solid, carbonized, and annealed Pressed Graphite Pebbles (PGP). We also received one Annular Surrogate Pebble (ASP) with surrogate oxide particles pressed into the annular fuel region with a 37% packing fraction. This pebble was carbonized but not annealed. The configurations of these two types of pebbles are illustrated in Figure 21(a) and Figure 21(c) respectively.

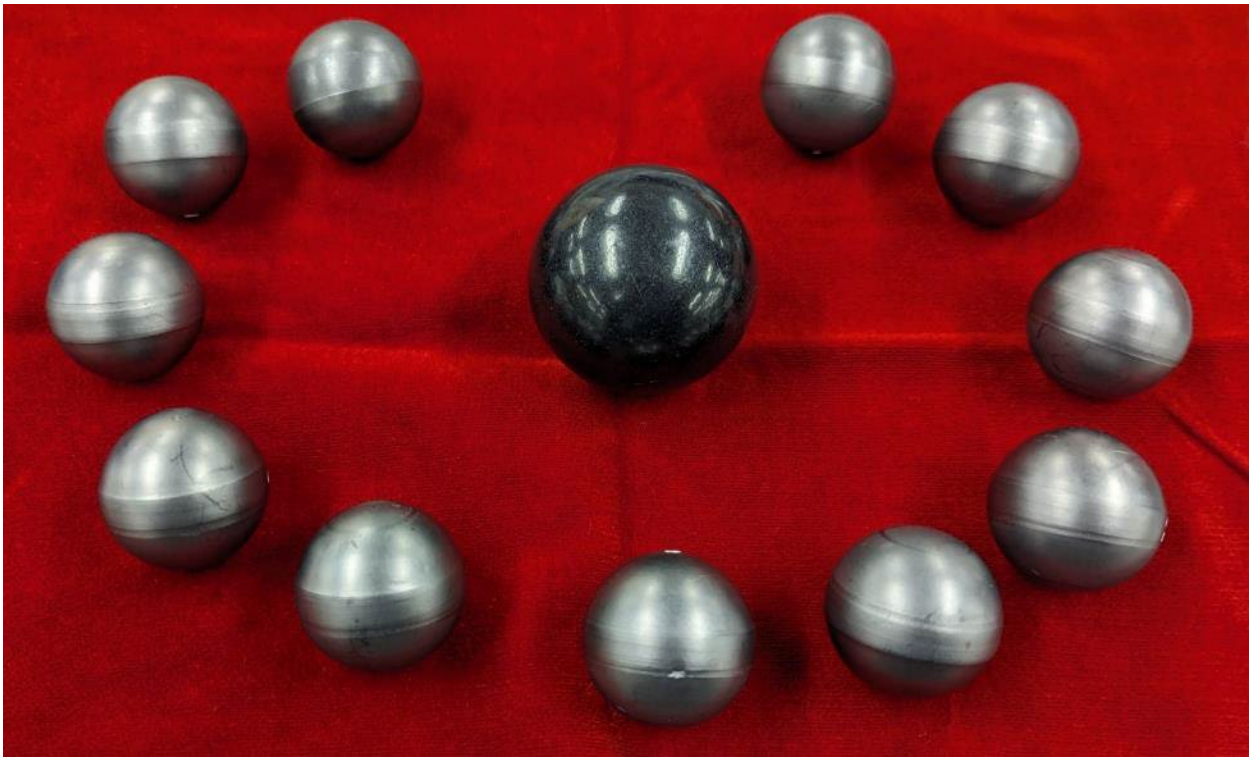

Figure 20. All pebbles inspected with ECT.

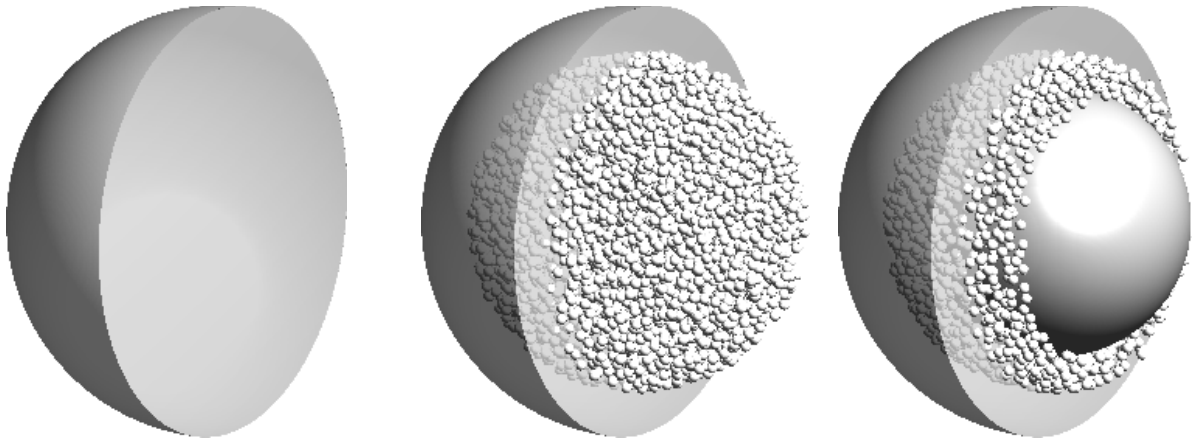

(a) (b) (c)

Figure 21. Pebble configurations. Shown here are (a) a solid pebble, (b) a regular filled fuel pebble, and (c) an annular fuel pebble.

In order to confirm pebble configurations, X-ray radiographs were collected on all pebbles using SINDE's X-ray facility. Sample radiographs on a solid pebble and an annular pebble are shown in Figure 22. Although the system can provide up to 420 kVp (kilovolts-peak), a tube voltage of 26.5kVp was sufficient to penetrate through the solid pebble, as shown in Figure 22(a). However, the density of surrogate particles in the annular pebble blocked the penetration of X-rays generated at that voltage, as shown in Figure 22(c). In order to penetrate through the annular fuel region, the tube voltage was increased to 110kVp. The solid pebble is practically transparent at this energy level, as can be seen in in Figure 22(b), shown here with a calibration standard for accurate measurement of width. The radiograph in Figure 22(d) confirms that the ASP pebble matches the annular configuration in Figure 21(c). Radiographs were collected at 3 angles for each pebble; however, detection of fine cracks was difficult without accurately aligning the pebbles to the locations of suspected cracks. Future work might involve X-ray tomography in addition to radiography if it is of interest to involved parties.

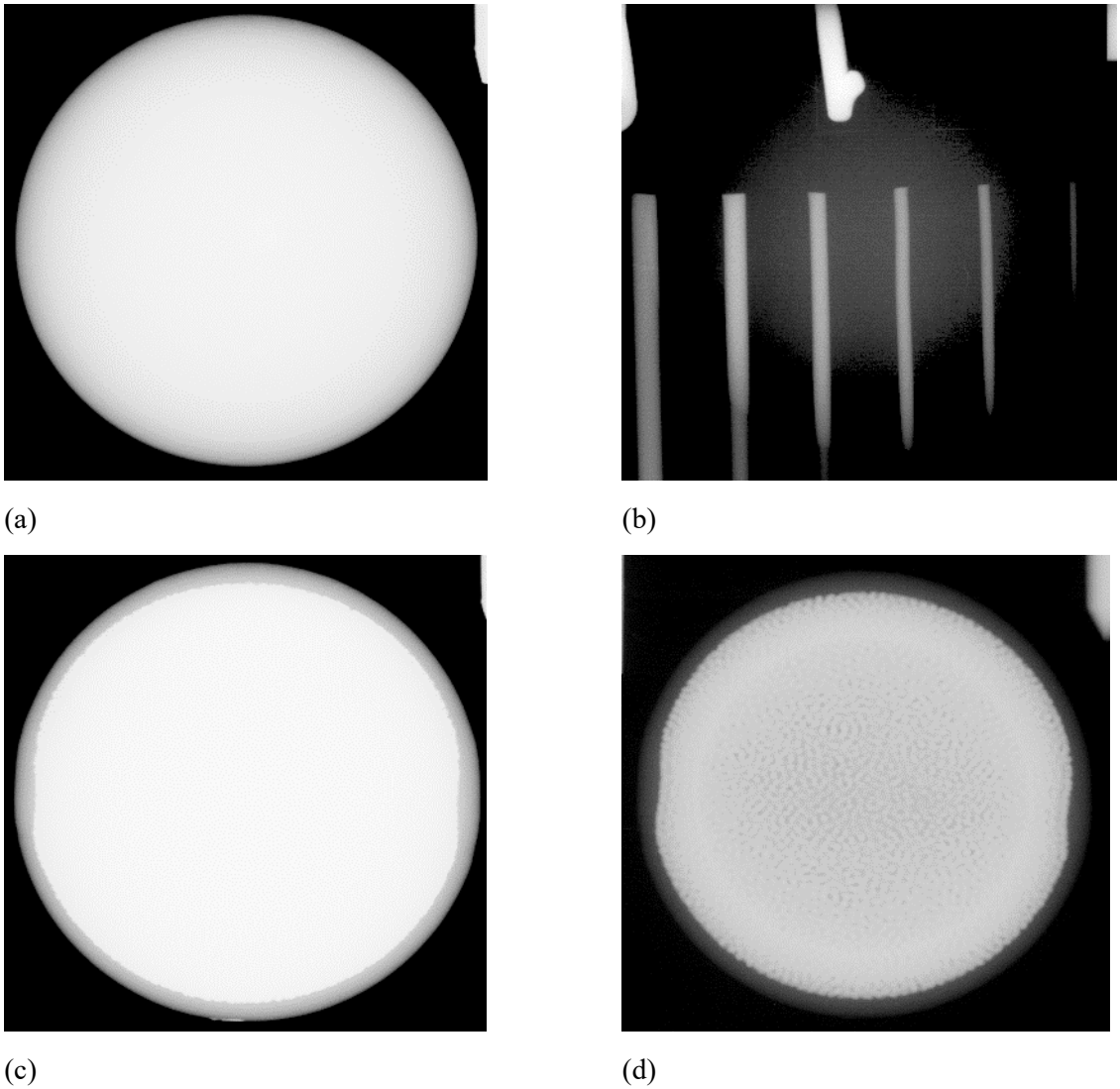

(a) (b)

(c) (d)

Figure 22. Sample X-ray radiographs on a solid and an annular pebble. Shown here are (a), (b) a solid pebble and (c), (d) an annular pebble. X-ray radiographs are collected using (a),(c) 26.5kVp and (b),(d) 110kVp tube voltages.

2.3.5 Flaw Detection

Using the lift-off calibration, as illustrated in Figure 11, the coordinate system is transformed such that the lift-off of the probe is predominantly along the horizontal axis and therefore signals that show a vertical component are more likely to be flaws, such as cracks. In typical eddy current examination, the phase rotation of the signal is one way to estimate the depth of the flaw, assuming one has a calibration sample to generate the depth vs phase response of the probe. However, since the amplitude of the signal also depends on the volume of the flaw (width, depth, length), amplitude can also be used as a surrogate to estimate relative depth for similar flaws.

EC data were collected on all pebbles in Group 2 using single-frequency techniques at 1000 kHz, and at 500 kHz to maximize gain. Data files were also collected in a four-frequency technique using 1000 kHz,

500 kHz, 250 kHz, and 50 kHz frequencies, but at a lower gain. As expected, 1000 kHz gave the best response for surface-breaking cracks in the pebbles. Due to the variation between coils, some basic filtering was applied to all datasets to help align the data. The most common tool used was a median-subtraction filter. Furthermore, since data was oversampled for possible future use, a resampling filter was also applied to make data analysis easier. It should also be noted that the array probe technique used favored detection of vertical cracks over detection of horizontal cracks.

Some examples of flaw detection using ECT along with conformation photographs are shown in the following figures. Figure 23 shows a pebble in which an obvious dent is visible on the surface. EC data confirmed the dent, along with detecting a nearby feature. Since the dent is primarily a lift-off signal, i.e., the surface of the pebble falls away under the probe, the dent signal shows up in the horizontal component of data shown in Figure 23(c), but not in the vertical component shown in Figure 23(d). However, the other nearby feature does show up in Figure 23(d), indicating that it is crack-like. Closer photographic inspection of the pebble confirms a nearby crack, shown in Figure 23(a).

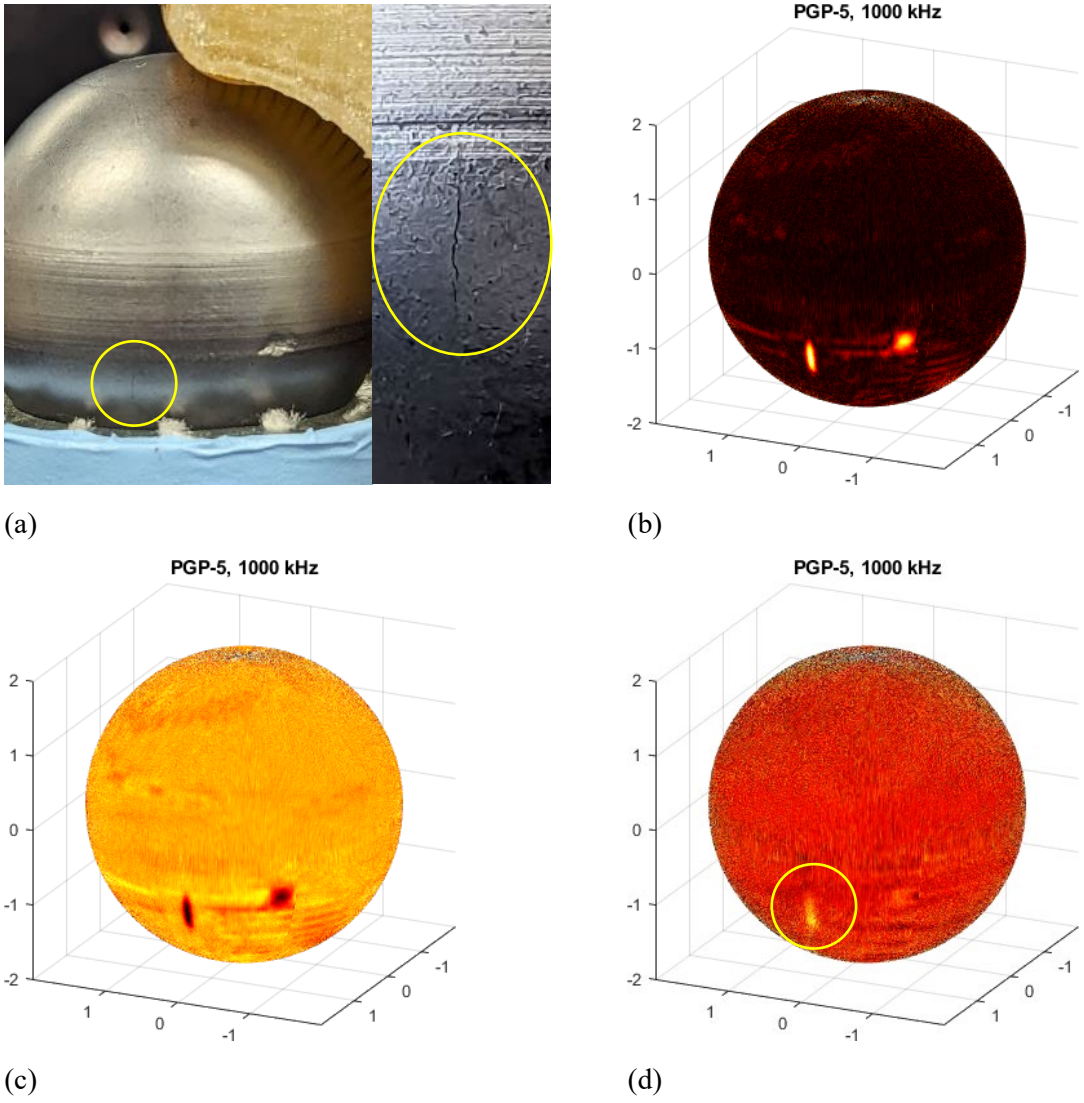

Figure 23. Flaw detected in pebble PGP-5. Shown here are (a) photographs of the pebble, (b) amplitude of EC data, (c) horizontal component of EC data, and (d) vertical component of EC data.

The pebble labeled as PGP-7 also exhibits multiple flaws, as shown in Figure 24 and Figure 25. As with PGP-5, closer photographic inspection reveals surface-breaking cracks in this pebble. While the first crack in Figure 24 is fairly easy to detect with the naked eye, the crack found in Figure 25 was not visible to the naked eye, but showed up with camera magnification.

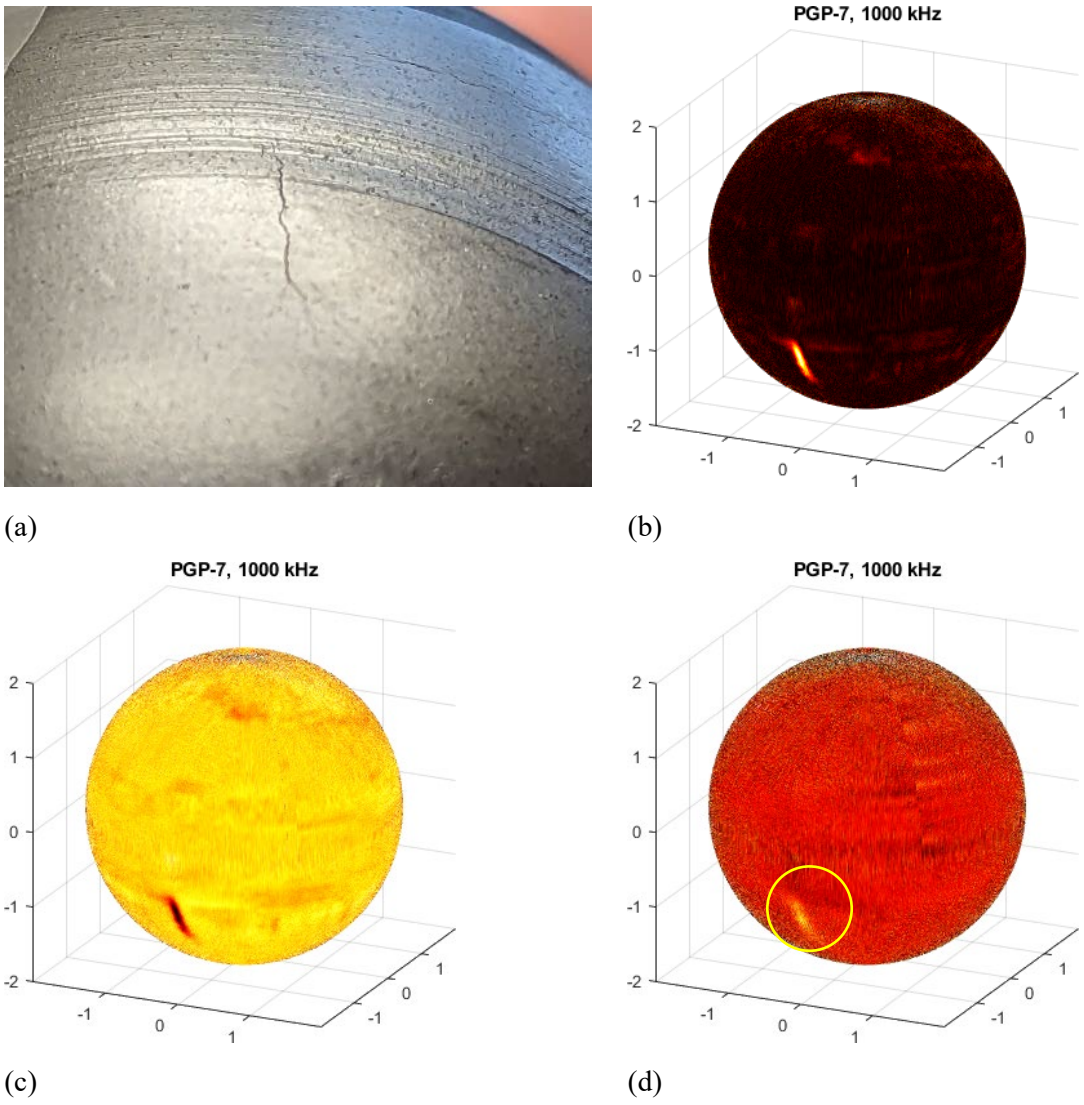

(a) (b)

(c) (d)

Figure 24. Flaw detected in pebble PGP-7. Shown here are (a) a photograph of the pebble, (b) amplitude of EC data, (c) horizontal component of EC data, and (d) vertical component of EC data.

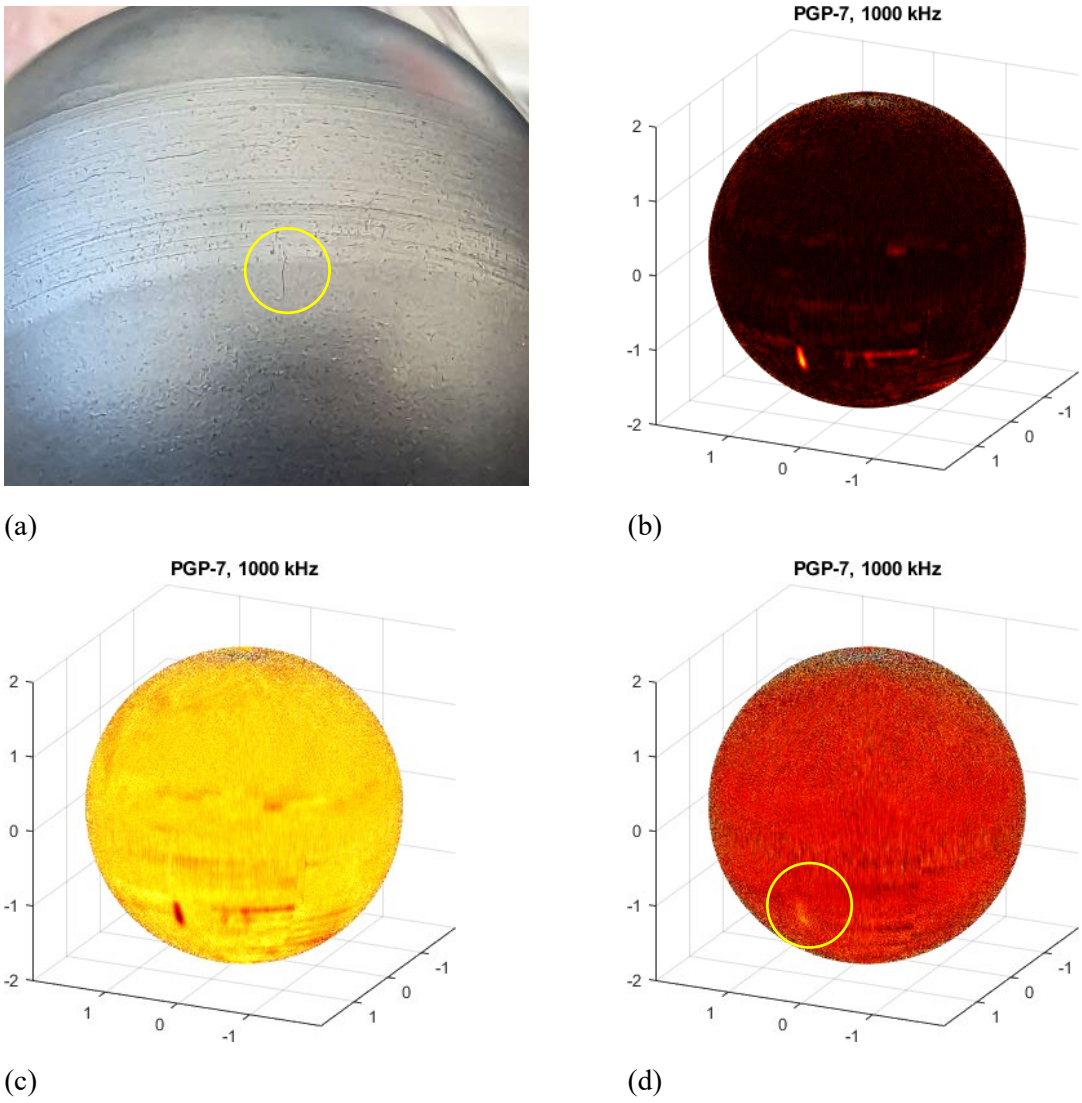

Figure 25. Smaller flaw detected in pebble PGP-7. Shown here are (a) a photograph of the pebble, (b) amplitude of EC data, (c) horizontal component of EC data, and (d) vertical component of EC data.

Another crack found with EC and the confirming photo are shown in Figure 26, this time in PGP-8. More than half of the PGP pebbles exhibited cracking either immediately above or immediately below the equatorial band of the pebble. In general, the flaws only show up on one side of the band, which could be indicative of a manufacturing defect. Since there were no distinguishing marks on the hemispheres, top and bottom were chosen arbitrarily, so that cannot be used as a true difference. More detailed EC inspection data on all pebbles in Group 2 can be found in Appendix A.

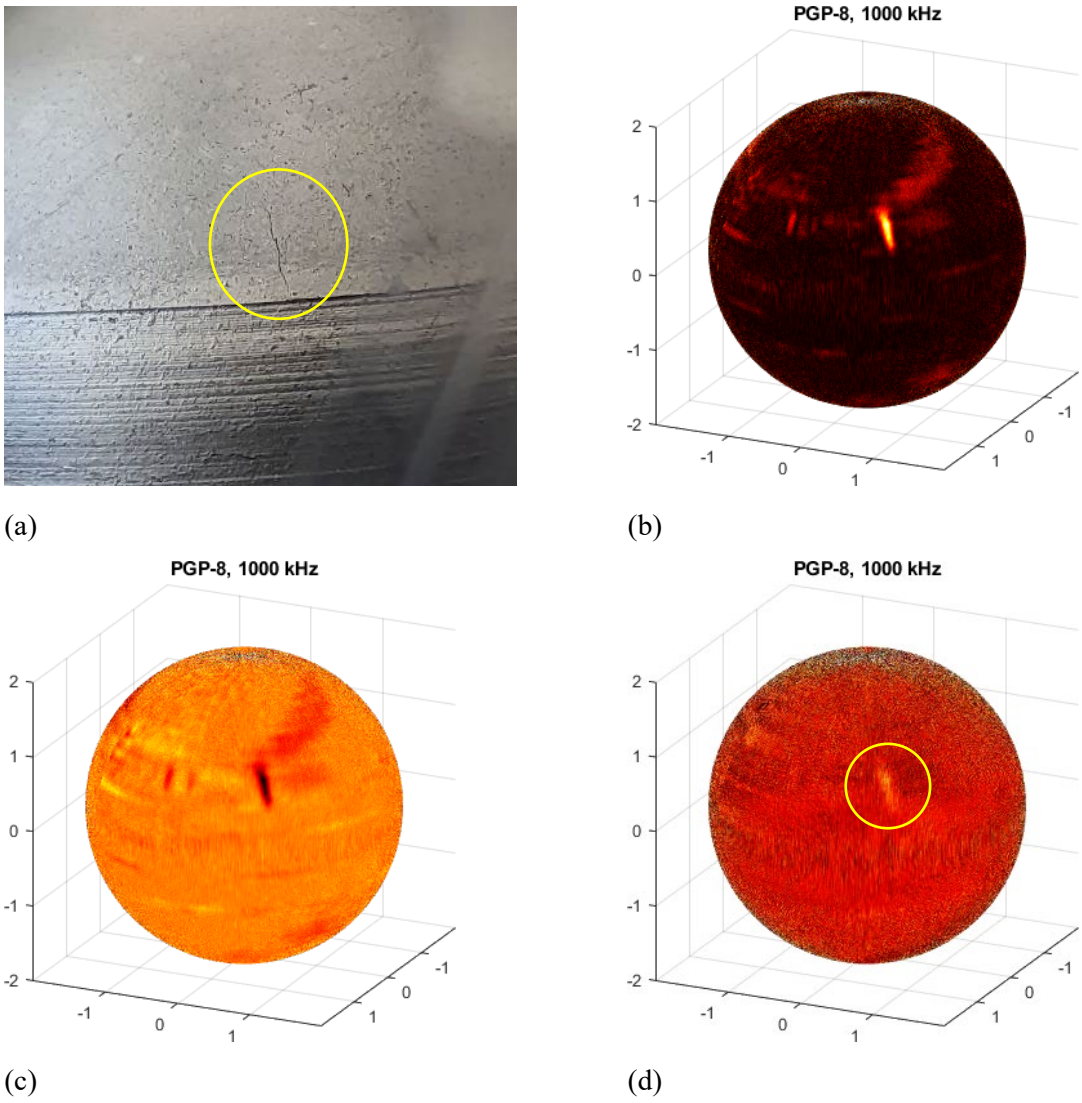

Figure 26. Flaw detected in pebble PGP-8. Shown here are (a) a photograph of the pebble, (b) amplitude of EC data, (c) horizontal component of EC data, and (d) vertical component of EC data.

2.3.6 Distinguishing between ASP and PGP

There is vendor-stated interest in identifying pebbles by batch and type. Certain High Temperature Reactor (HTR) designs use an annular core configuration [9]. This configuration arranges absorber material both in the central column and on the side (so-called 'dummy' pebbles) while the fissile pebbles are in between. This configuration provides a higher ratio of surface area to volume, which assists the passive transfer of the decay heat to the heat sink. Being able to rapidly identify and return these dummy pebbles to circulation would be one use for this capability. Similarly, being able to sort active pebbles by batch would allow newer pebbles to return to circulation without needing to check for activity.

Measurements were taken using a pencil probe on ASP and PGP pebbles. Since lift-off calibration depends on the material under examination, data used to sort materials are displayed before this type of calibration is applied. As can be seen in Figure 27, the EC method used in this work can readily distinguish between

these two types of pebbles using K-means clustering. K-means clustering is a method that aims to categorize points into K groups in which each point belongs to the group with the nearest mean. All the solid pebbles in Figure 27(a) fall in one group, while the annular pebble falls into another cluster. The third group is then the signal in air. The time trace in Figure 27(b) shows the capability to group measurements in real-time. This clear differentiation in the EC signals is likely due to the annealing process, which was not performed on the annular pebble, thus causing a difference in conductivity. However, it is believed that even if the pebbles use the same annealing process, using a frequency with a great enough penetration depth will be able to still separate pebble types based on the presence or absence of the embedded fuel particles, which will modify the conductivity in the annulus layer.

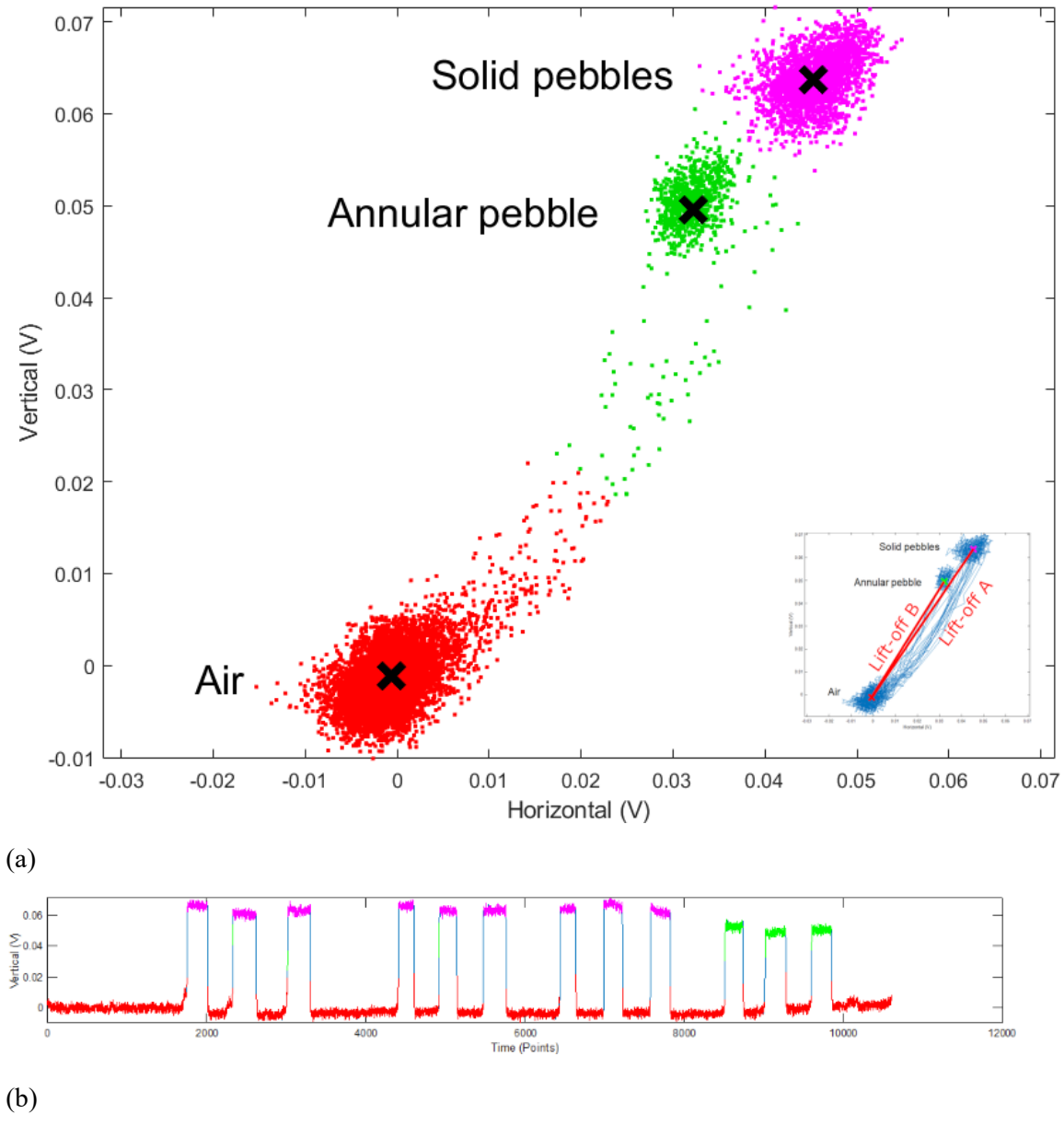

Figure 27. Distinguishing between ASP and PGP. Shown here are EC data (a) on a complex Lissajous plot and (b) strip chart of the vertical component of the data.

2.4 Eddy Current Observations

From our VIM simulations, we made several observations. If the conductivity of a graphite pebble is in the range described in Reference [11], a frequency between 500 kHz and 1000 kHz would be optimal. However, if the conductivity of the pebble is in the lower range for graphite, operating at higher frequencies would be more advantageous. Experimental data showed that the pebbles we received were in the lower conductivity regime. This directed us to using higher frequencies and probe designs which produce higher current flux density (CFD). Thus, the frequency we chose for analysis was 1000 kHz. Data acquired in the laboratory confirmed the utility of this higher frequency for near-surface flaw detection. Lower frequencies may still be desired for greater depth of penetration. Simulations also showed that while a 6 mm diameter coil may produce a stronger signal, the difference of a single order of magnitude between 6 mm and 3 mm coils at 4.5 mm depth may be an acceptable tradeoff to achieve higher resolution.

Scans collected on the original 4 cm pebble seemed to indicate a near-surface feature could be found in one hemisphere of the pebble. The pencil probe also seemed to indicate another feature in the other hemisphere, but the non-reproducibility of the phase and amplitude of this feature led to a low level of confidence in feature classification. This feature also did not show up in the array probe data. The non-reproducibility of the array probe data in general was largely attributed to the difficulty in manual positioning of the probe. This was addressed by 3D printing a custom probe mount to conform to the pebble's surface, which was used for scans of Group 2 pebbles.

Scans on pebble PGP-5 showed a detectable denting feature on the surface and a nearby crack. The EC data was effectively able to differentiate between the two flaw types. More than half of pebbles in Group 2 exhibited vertical cracks, primarily at the edge of the equatorial band. The consistency of locations of the cracks seems to indicate they arise from the manufacturing process. While horizontal cracks in the equatorial band were observed by visual inspection, the nature of the data collected, and the data processing used, somewhat hindered the detection of these flaws. This can readily be resolved by using a different multiplexing scheme when collecting data or by rotating the pebbles 90°.

Due to annealing differences, the material properties were sufficiently different to distinguish between ASP and PGP using K-means clustering. The change in material properties due to annealing is a dominant factor in the difference between the EC signals on the two pebble types. However, it is believed that, even if the pebbles use the same annealing process, using a frequency with a great enough penetration depth will be able to still separate the pebble types based on the presence or absence of the embedded fuel particles, which will modify the conductivity in the annulus layer.

3 Thermal Imaging

The following section details simulated and experimental research on the cooling behavior of heated graphite pebbles to better understand thermal properties for artefact identification and location purposes. For the modeling work, we studied the effect of internal defects on the surface temperature profile of pebbles as they cool down to room temperature. The basic premise of the research was that the internal defects (e.g., internal pores) will alter the heat flow within the pebble, leading to surface temperature profiles which are unique to a pore geometry, and since the pore geometry in each pebble is unique to that pebble, the surface temperature distribution can be used as an indicator of individual pebbles. The experimental aspect of the work focused on potential differences between the surface temperature of two types of pebbles. For that, individual pebbles were heated up in an oven, and then were taken out from the oven to cool down. Thermal imaging was used to study potential differences between their surface temperature distribution and its changes with time. Moreover, we studied the impact of surface defects (holes drilled on the pebbles) on the surface temperature distribution. The work described herein was conducted at TAMU within their thermal imaging laboratory.

3.1 Heat Flux Modeling

The heat transfer in pebbles with embedded spherical cavities were modeled via finite element analysis (FEA) in a commercial software, ANSYS. Surrogate graphite pebbles (like those described in section 2) were modeled with a diameter of 40 mm and cavity diameters of 2 mm and 1.5 mm. The closest point of the surface of the cavity to the outer surface of the cavity, *the cavity depth*, was 1 mm. When modeling the pebble, the material properties of graphite were considered from the ANSYS material library. The material properties of air were also considered since the pebbles were allowed to cool down in air. The convection coefficients used for the modeling were 100 and 200 W/m^2°C (assuming moderate and severe air-flow induced cooling). The initial temperature was set at 100° C throughout the pebble, and the pebbles were allowed to cool down with convection in air (surface boundary condition was convection). The ANSYS solver solved the transient heat transfer equation (Equation 3) below.

$$\rho c_\rho \frac{\partial T}{\partial t} - \nabla \cdot (k \nabla T) = 0 \qquad (3)$$

Respectively, ρ, c_ρ and k are the mass density, specific heat capacity and thermal conductivity of the pebble, and T and t are respectively the local temperature in the pebble as a function of time. An example of the modeling result is presented in Figure 28.

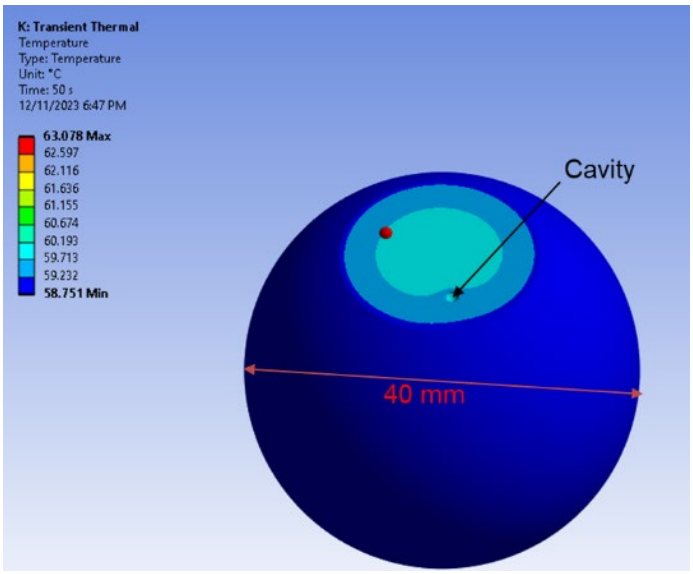

Figure 28. Transient temperature distribution in a pebble with an internal cavity.

Though theoretical, the interior of the pebble will not be accessible in an equivalent experiment. Hence, the FEA models only studied the surface temperature of the pebbles near and away from the cavity. From the FEA analysis, it appears that the presence of the cavity slows down the cooling rate at the initial stages of the cooling (right after the convective heat loss is activated in the model) at points near the cavity compared to points away from it . This is mainly due to the presence of the cavity reducing the heat flux in the cavity. However, as the temperature of the surface reaches ~45 °C, the rate of cooling slows down considerably, and the rate of cooling on the surface of the pebble near the cavity is slightly higher than the other surface points. That is mainly because the faster heat loss at the beginning of the cooling process lowers the temperature gradient with the surrounding air.

Overall, it seems that the presence of the cavity has little impact on the surface temperature distribution of the pebble. As an example, the variation in temperature of the pebble surface as a function of time just above and away from the cavity are shown in Figure 29(a). In this plot, it is very difficult to notice the difference between the two temperatures. Hence, we plotted the difference between the two temperatures as a function of time in Figure 29(b). As expected, the temperature difference initially rises as the surface points above the cavity, but eventually, the temperature difference goes to zero as the whole pebble reaches equilibrium with the environment.

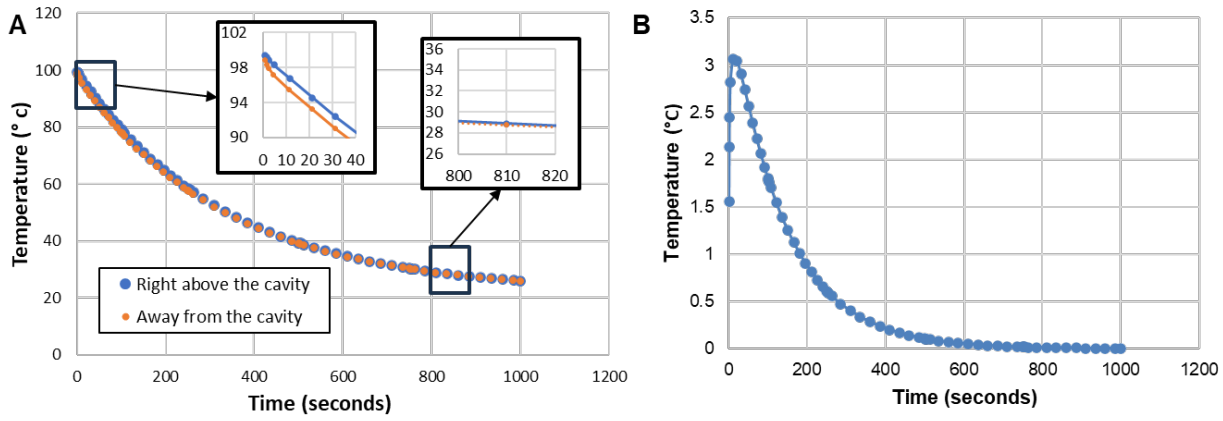

Figure 29. A. The variation of the surface temperature vs. time for a point right above the cavity and away from that. B. The difference between the two temperatures as a function of time (a cavity with a diameter of 2 mm, embedded 1 mm below the surface).

In the case of a cavity with a diameter of 1 mm which was embedded below the surface of the pebble, the maximum temperature contrast on the surface was 1.39 °C. This value was greater for the case of 2 mm diameter hole where the maximum temperature contrast was 3.06 °C (as shown in Figure 30).

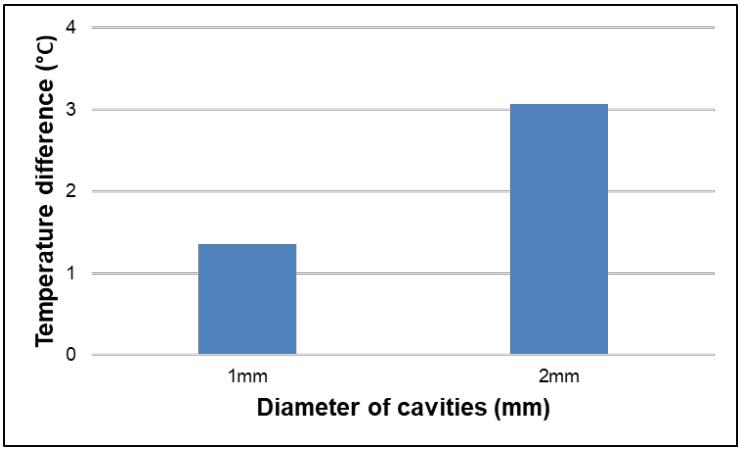

Figure 30. The surface temperature contrast as a function of the size of the cavity.

We also studied the effect of forced convection on the cooling rate and the temperature contrast in the pebbles. As an example, we modeled the temperature contrast in a pebble with an embedded cavity of 1.5 mm 1 mm below the surface, and we considered two heat convection coefficients of 100 and 200 W/m^{2}C. As expected (see Figure 31), the increase in the forced convection coefficient increases the temperature contrast as the heat flux on the surface goes up with higher heat convection coefficient.

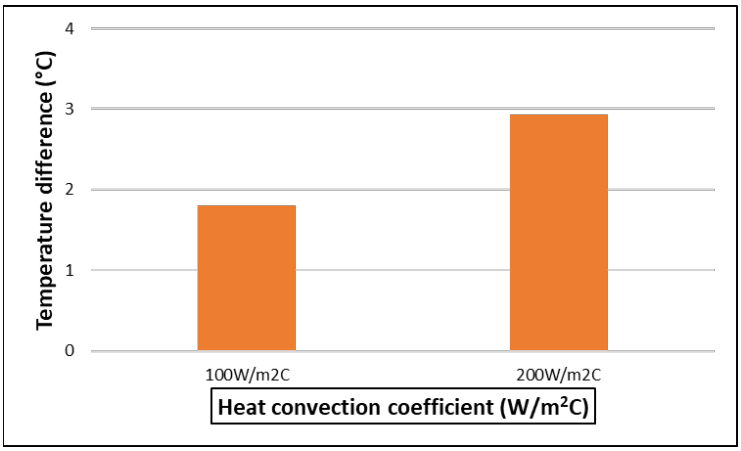

Figure 31. The magnitude of the surface temperature contrast as a function of heat convection coefficient (cavity diameter ~1 mm).

3.2 Experiments on thermal imaging of the pebbles

Six individual pebbles of PGP and one of ASP were all 4 cm in diameter and manufactured of graphite. To study the heat transfer in pebbles, they each were heated up to ~110 °C in a convection oven. After they reached thermal equilibrium with the oven, they were taken out, placed on a glass base, and imaged with a thermal camera. An image was captured every 60 seconds until the pebble reached near-room temperature (27 °C). An example of the experiment is shown in Figure 32 (while images were taken at every 60 seconds, sample images at every 300 seconds are presented below).

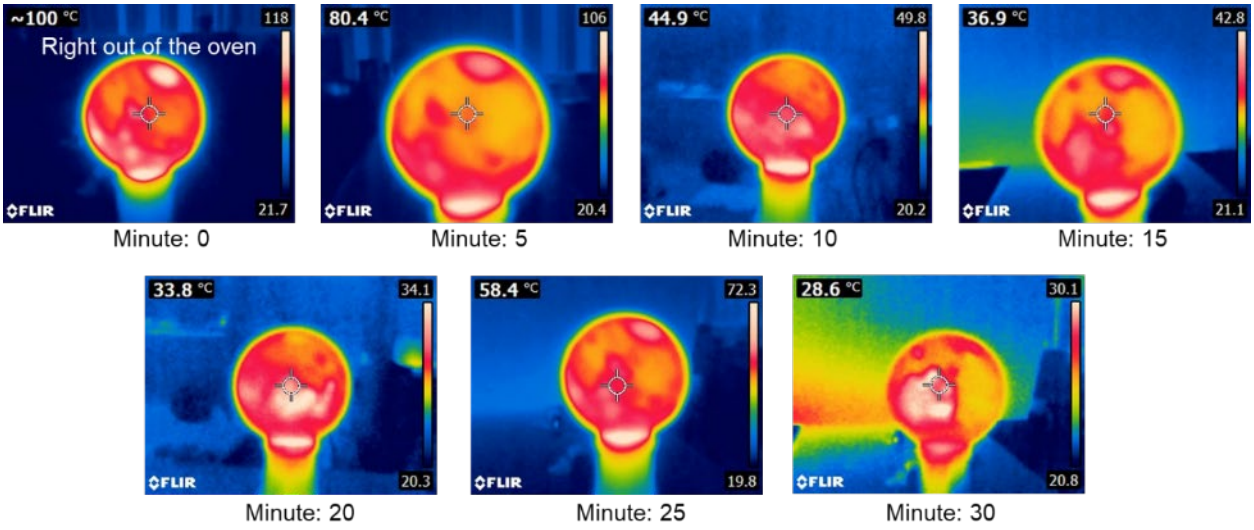

Figure 32. Thermal images with time snapshots.

First, we evaluated the uniformity of surface cooling on the pebbles. To this end, we measured the temperature of two distant surface points of the pebble (referred to herein as front and side view of the pebble) and plotted them against time. We also measured the transient temperature drop in various PGP pebbles and also plotted them against time. As shown in Figure 33, the temperature variations of distinct

points in a pebble and also five individual pebbles of the same type (PGP) as a function of time are very similar, indicating the repeatability of the temperature measurements on the surface of the pebbles via thermal camera. At the beginning of the experiment, this was a concern as reflections of the light from the surface of the pebbles could have influenced the thermal imaging. However, the experimental results indicate the reliability of the thermal imaging in assessing the surface temperature of the pebbles.

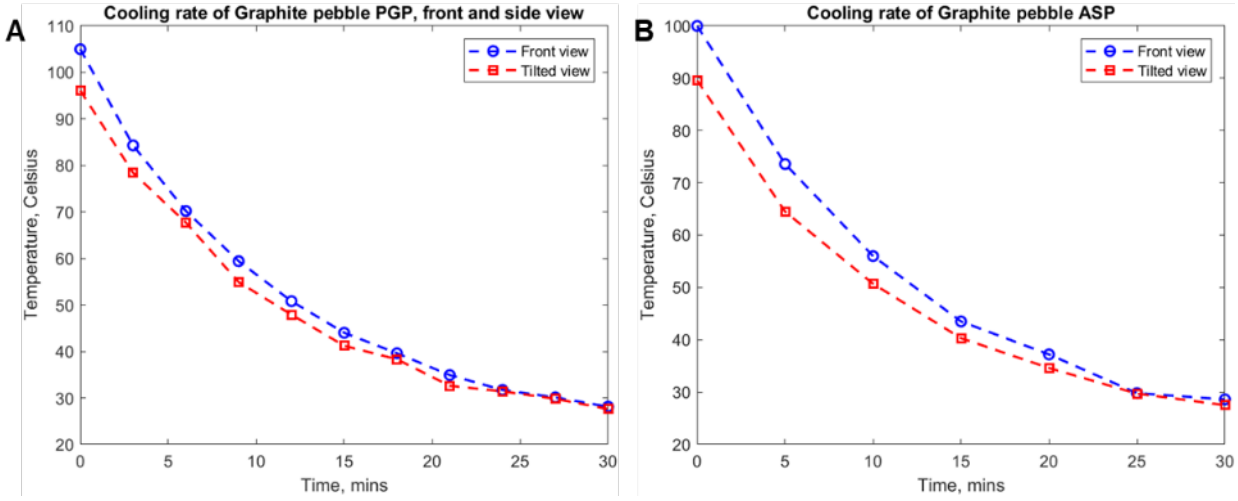

Figure 33. Front and side view temperature of the pebble as a function of time of A. PGP and B. ASP pebbles.

We proceeded with measuring the temperature changes in different pebbles, namely the PGP and ASP. The experimental procedure was the same, and the results are shown in Figure 34. The measured temperature variations were further manipulated to better reflect the physics of the heat transfer which governs the cooling of the pebbles. To this end, the rate of heat loss in the pebble was related to the heat flux on the surface due to heat convection:

$$mc\frac{dT}{dt} \approx -hA\left(T - T_{inf}\right) \qquad (4)$$

In Equation 4, m is the mass of the graphite pebble, c is the specific heat of material, h is the heat transfer coefficient, A is the surface area ($4\pi r^2$) of the pebble with r = 2cm. Therefore,

$$\frac{dT}{dt} \approx -\frac{hA}{MC}\left(T - T_{inf}\right) \quad (5)$$

Here, we have assumed that the whole pebble cools down uniformly. Hence, the rate of change of the surface temperature was plotted against the difference between the surface temperature and that of the surrounding air (T_{inf}). From Figure 34(b), it is evident that the change in the temperature of the PGP and ASP pebbles are very similar to one another, or at least the difference is not statistically significant.

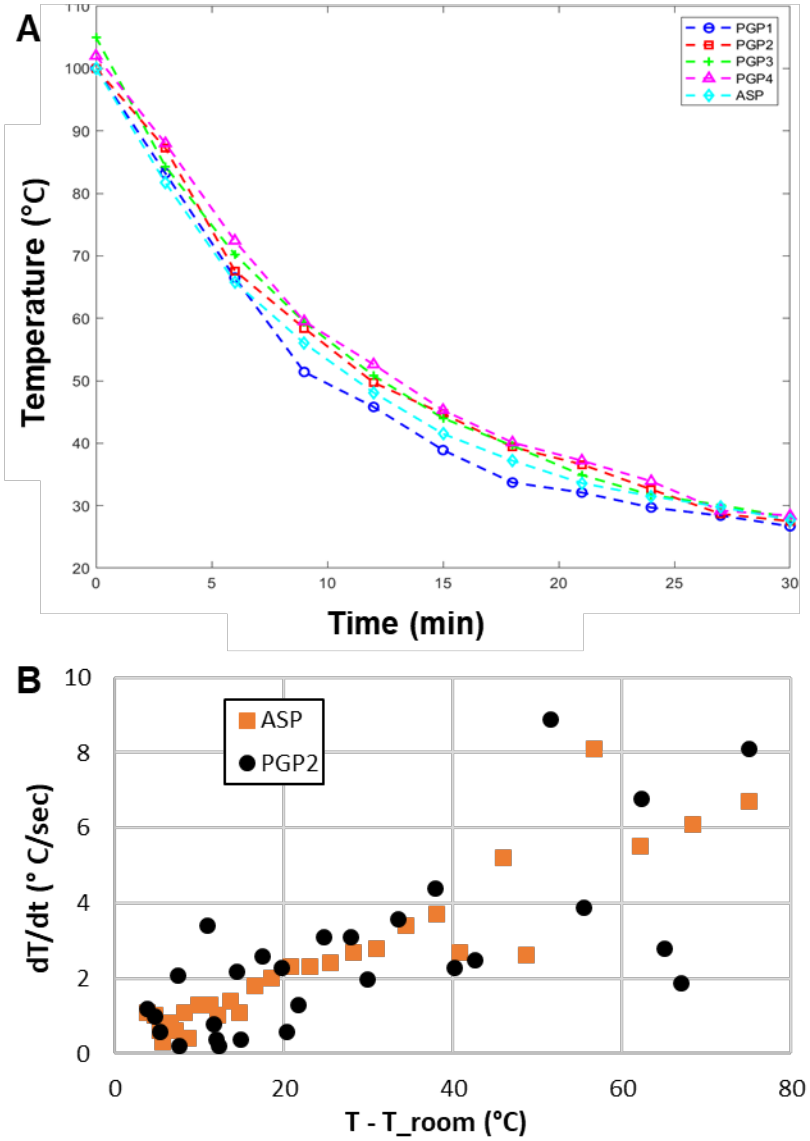

Figure 34. A. Surface temperature vs. time for PGP pebbles. B. The rate of change in temperature vs the temperature gradient with air for PGP and ASP pebbles.

3.3 Thermal Imaging of Pebbles with Defects

Based on the initial pebble monitoring design of the system and with feedback from PBR designers, we evaluated the effect of defects on the temperature distribution of the surface of the pebble. This could support pebble identification for tracking of PBR fuel through the reactor or to potentially identify defective pebbles during operation. To this end, holes were made in PGP pebbles via drilling. The diameter of the holes were 1.5 mm and 2 mm and consisted of various depths: 1 mm, 2.5 mm, and 3 mm. Each pebble was then heated up in an oven to ~110 °C and the rate of cooling between surface points near and away from the drilling site was studied via thermal imaging. An example of the thermal images obtained during the cooling of one of the pebbles with 2 mm wide and 3 mm deep hole is shown in Figure 35. It is clear from the images,

that the presence of the hole has a notable impact on the temperature of the surface and delays the heat loss – perhaps due to the air inside the hole acting as a low heat conductivity medium delaying heat loss.

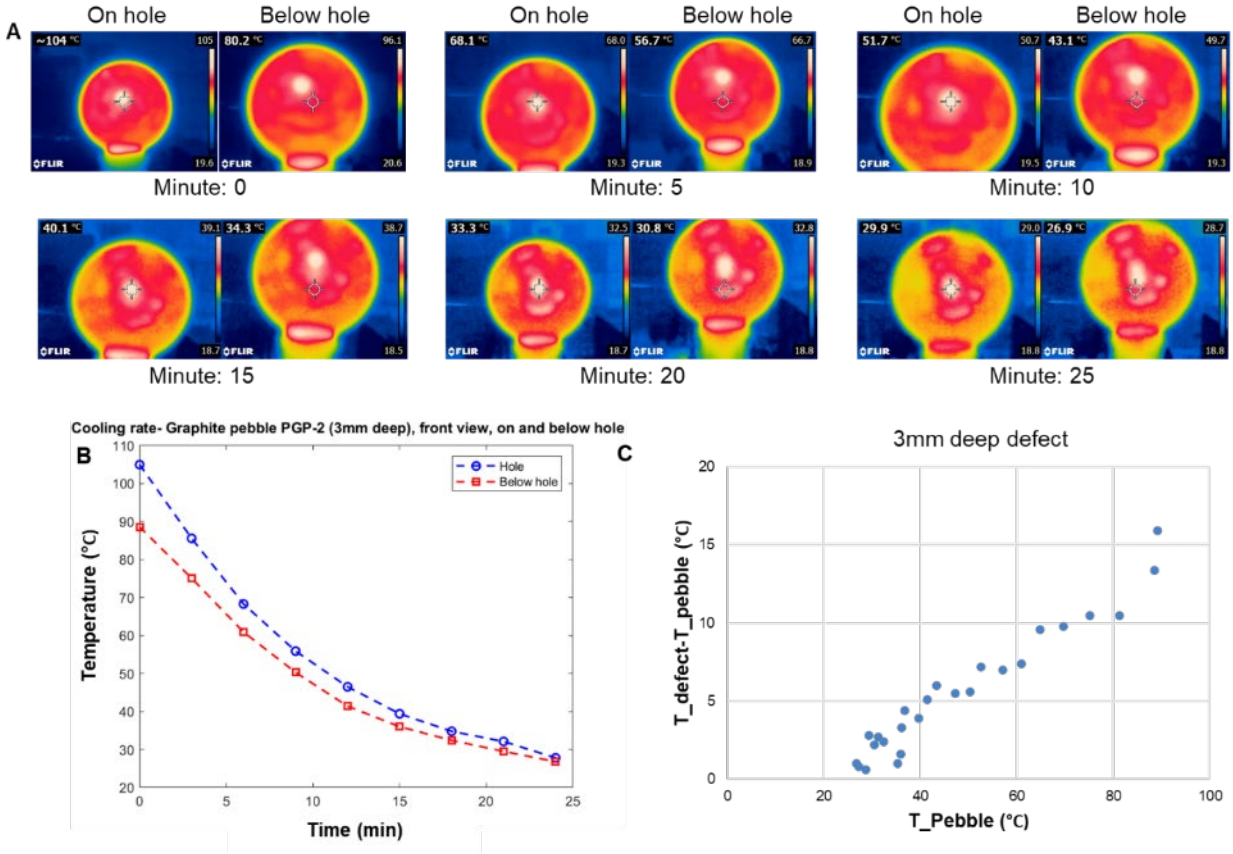

Figure 35. A. Thermal images with time snapshots of a pebble with a drilled surface hole (right out of oven, 1 minute, 5 minute, 10 minute, 20 minute, 25 minute). B. The variation of the temperature with time for a point right at the defect and a point away from that. C. The temperature difference between a point near and away from the defect.

The temperature difference between the surface points at the defect and away is a function of time and approaches zero at sufficiently long times as the pebble reaches thermal equilibrium with the environment. However, the temperature difference during the cooling process may reach 5°C to 15°C at its peak, depending on the size and depth of hole. The maximum temperature difference occurs at the early stages of cooling and in the first few minutes. The dependence of this maximum temperature difference on hole diameter and depth is as follows. As conveyed in Figure 36, for a hole with a diameter of 1.5 mm (3 mm deep), the maximum temperature difference is ~11.7 °C, while for a hole with a diameter of 2 mm (33 mm deep) is ~15.9 °C. In other words, a wider hole seems to increase the temperature contrast. This is expected, as the wider hole traps a larger body of air with its very low thermal conductivity. In contrast, for holes with the same diameter, the depth of the hole does not seem to be an important factor in increasing the temperature contrast in the range studied (1 mm – 3 mm). It is perhaps the case that the reduced heat conductivity of the larger body of air that is trapped inside deeper holes are compensated for by the conduction in the graphite around the hole.

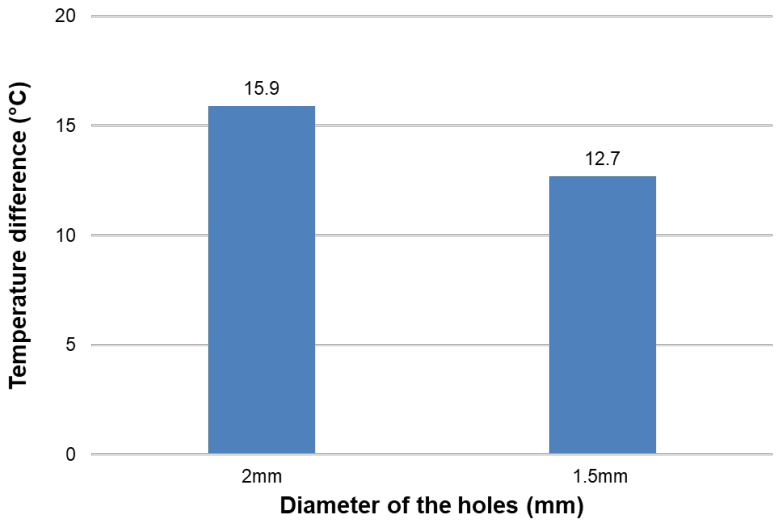

Figure 36. Maximum temperature difference between a point near the hole and away from it for two cases of a 1.5 mm and 2 mm wide holes (both 3 mm deep).

3.4 Thermal Imaging Observations

Based on the results presented above, the following observations were made:

1. Based on the finite element modeling results, the presence of cavities in a hot pebble that is exposed to surface temperature loss (e.g., via convection) results in a surface temperature contrast which initially increases with time but then fades away. At its peak, the temperature contrast may reach an amplitude of a few degrees Celsius, depending on various factors such as heat convection coefficient, thermal properties of the pebbles, size of the cavity and its proximity to the surface. Generally, cavities must be close (within mm) to the surface to generate a noticeable contrast. This finding is purely based on models, as the pebbles with cavities were not available, and extending the results to real case scenarios requires prior knowledge about the exact values of the pebble properties and geometry.
2. The presence of surface defects, in this case holes that were drilled on the surface, even as small as 1-2 mm, will result in a considerable temperature contrast on the pebble as it cools down. It seems that the presence of the hole slows down the rate of heat loss, likely due to the low thermal conductivity of the air that is trapped inside the holes, keeping the environment around the hole hotter for longer period of time. This finding is notable in that surface defects are projected to occur on pebbles over time and thermal imaging could serve a role in helping monitor the structural integrity of pebble fuel in PBRs.

4 Conclusions

Rapid inspection of graphite pebbles is a challenging task that is of great interest from both safety and safeguards perspectives. Operational limitations restrict accessibility to the pebbles once they are extracted from the PBR core making radiation measurements difficult for identification purposes. Imaging techniques should be considered for assisting in identifying unique characteristics of individual or batches of pebbles but wet-coupling media cannot be used. Therefore, dry scanning techniques like thermal imaging or eddy current imaging must be considered for scanning pebble fuel leaving the rector core. In concert with burnup

measurements, we believe an effective and comprehensive material control and accounting approach can eventually be developed utilizing some pebble monitoring technique based on an imaging system capable of identifying individual, if not batches of, pebbles in an operational PBR. Thermal imaging and eddy current imaging are two methods that can contribute to a material control approach and their utility should be further considered in future PBR designs.

5 References

[1] S. Bakhtiari and D. Kupperman, "Modeling of eddy current probe response for steam generator tubes," Nuclear Engineering and Design, vol. 194, no. 1, pp. 57-71, 1999.

[2] S. Bakhtiari and T. W. Elmer, "Technical Letter Report on Development of Flaw Sizing Algorithms for Eddy Current Rotating Probe Examinations," U.S. NRC, ADAMS Accession Number: ML090690837, 2008.

[3] Scott Hower, Zetec, EddyFi, E-mail exchange, 14 June 2022.

[4] V. Sridhar, K. Chana and M. Pekris, "High temperature eddy current sensor system for turbine blade tip clearance measurement," in 12th European Conference on Turbomachinery Fluid dynamics & Thermodynamics, Stockholm, Sweden, 2017.

[5] S. Majidnia, R. Nilavalan and J. Rudlin, "A numerical study of the depth of penetration of eddy currents.," Insight-Non-Destructive Testing and Condition Monitoring, vol. 58, no. 3, pp. 129-134, 2016.

[6] M. C. Tanzi, S. Farè and G. Candiani, "1.4.4.1 Graphite," in Foundations of Biomaterials Engineering, Academic Press, 2019.

[7] B. Marinho, M. Ghislandi, E. Tkalya, C. E. Koning and G. de With, "Electrical conductivity of compacts of graphene, multi-wall carbon nanotubes, carbon black, and graphite powder," Powder Technology, vol. 221, pp. 351-358, 2012.

[8] R. W. Powell and F. H. Schofield, "The thermal and electrical conductivities of carbon and graphite to high temperatures," Proceedings of the Physical Society, vol. 51, no. 1, pp. 153-172, 1939.

[9] Q. Yang, N. Gui and X. Huang, "Effects of the central graphite column dimension and pebble size on power density distribution in annular core pebble-bed HTR," Int J Energy Res, vol. 46, no. 6, pp. 8076-8092, 2022.

6 Appendix: Eddy Current array probe scans of Group 2 pebbles

Datasets were collected using single-frequency techniques at 1000 kHz and 500 kHz to maximize gain. Data were also collected in a four-frequency technique using 1000 kHz, 500 kHz, 250 kHz, and 50 kHz frequencies, but at lower gain. The following figures present data collected at 1000 kHz.

When looking at the figures below, keep in mind that the data is calibrated using lift-off calibration, as illustrated in Figure 4-3. The coordinate system is transformed such that the lift-off of the probe shows predominantly in the horizontal axis and therefore signals that show a vertical component are more likely to be flaws, such as cracks. Notable crack-like signals are circled, and a few visual confirmation images are provided. In typical eddy current examination, such as tubing inspection, the phase rotation of the signal is one way to estimate the depth of the flaw, assuming one has a calibration sample to calibrate the depth vs phase response of the probe. However, since the amplitude of the signal also depends on the volume of the flaw (width, depth, length), amplitude can also be used as a surrogate to estimate relative depth for similar flaws.

Colormaps are scaled to common color limits to aid in direct comparison between pebbles. For example, all amplitude plots below are plotted with the same limits, so a signal that is brighter in one amplitude image can be assumed to have a higher amplitude than a dimmer signal in another amplitude image.

Orientation markers were created using correction fluid to aid in reproducing pebble orientation. This marker fluid is typically transparent to EC, however, it does occasionally show up as a lift-off signal at 270° longitude, 0° latitude, as can be seen in PGP-2 in Figure A-3 (a) and (b).

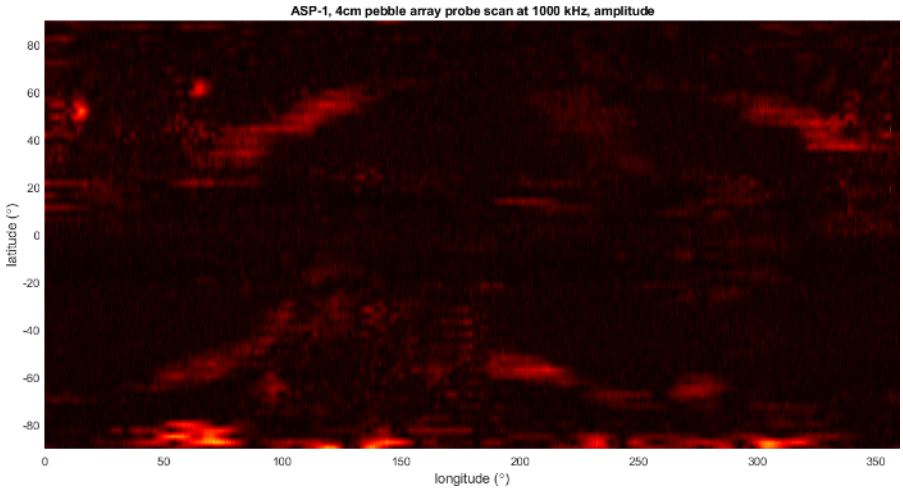
ASP-1, 4cm pebble array probe scan at 1000 kHz, amplitude
latitude (°)
longitude (°)

(a)

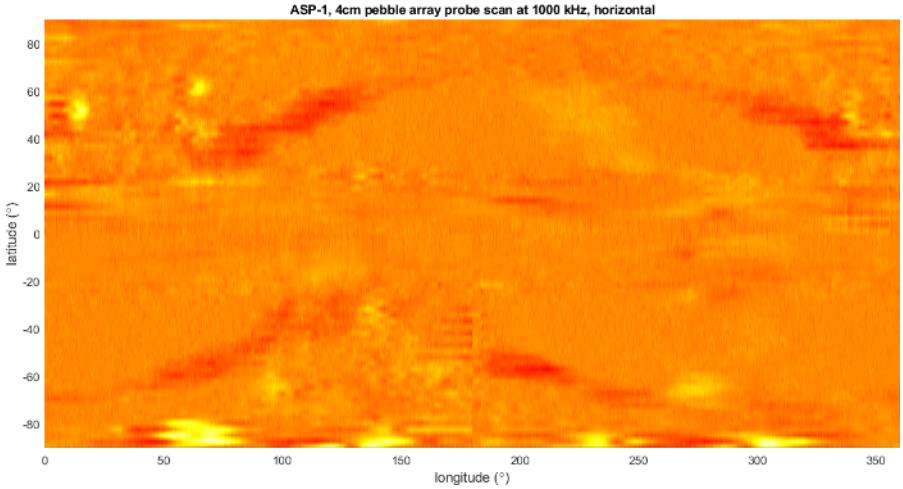
ASP-1, 4cm pebble array probe scan at 1000 kHz, horizontal
latitude (°)
longitude (°)

(b)

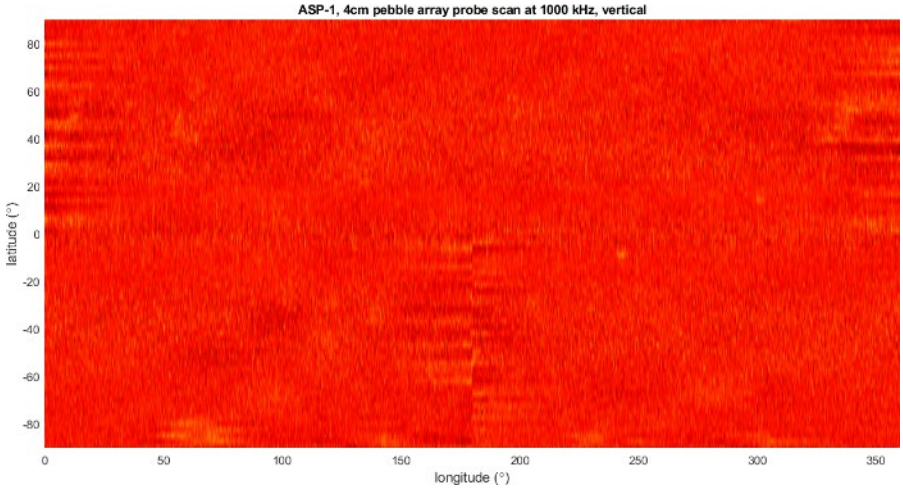
ASP-1, 4cm pebble array probe scan at 1000 kHz, vertical
latitude (°)
longitude (°)

(c)

Figure A-1. ASP-1. Shown here are the eddy current (a) amplitude, (b) horizontal component, and (c) vertical component.

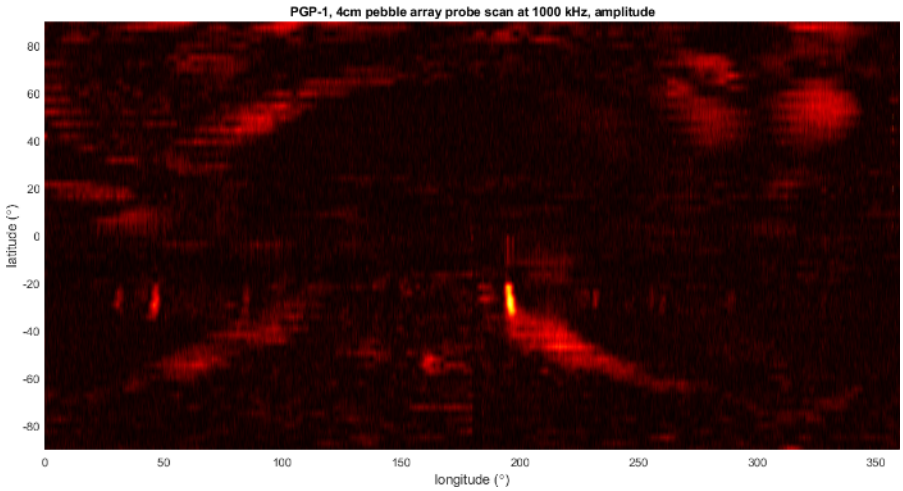

(a)

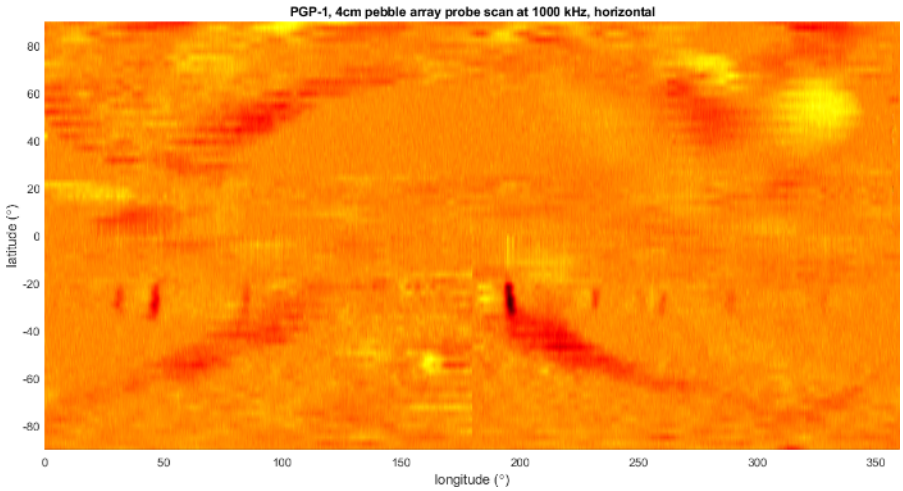

(b)

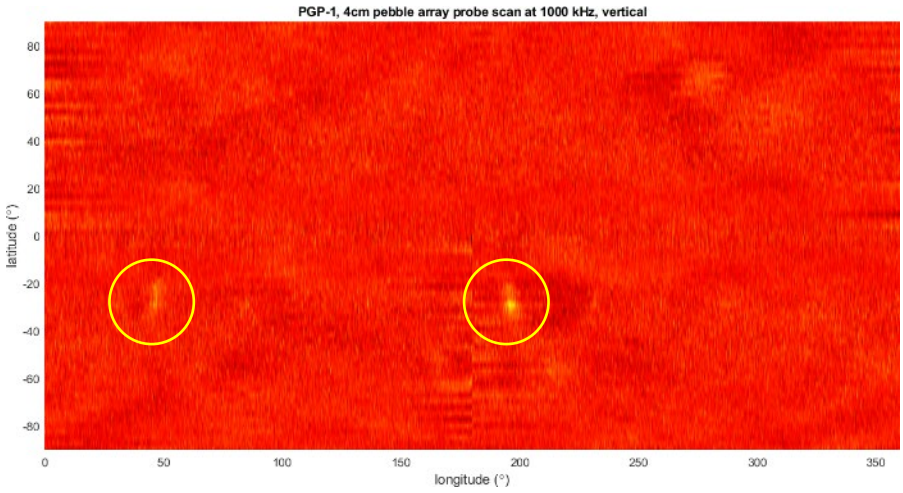

(c)

Figure A-2. PGP-1. Shown here are the eddy current (a) amplitude, (b) horizontal component, and (c) vertical component.

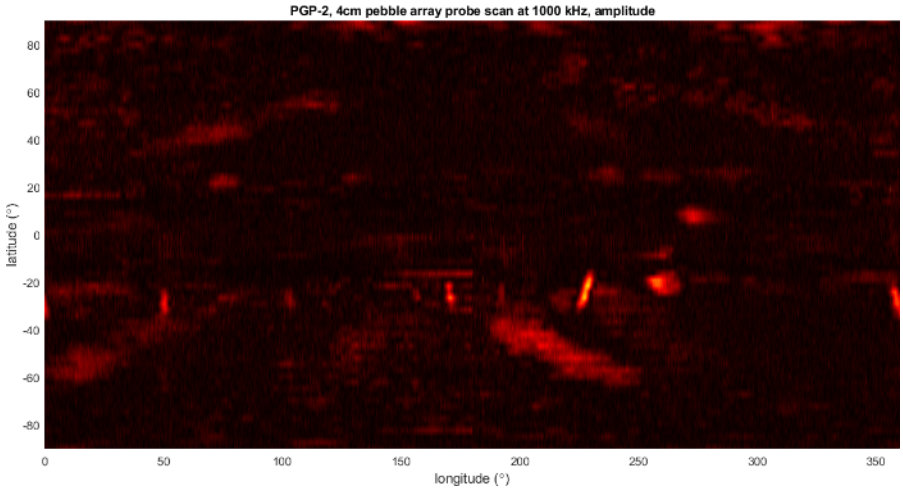

(a)

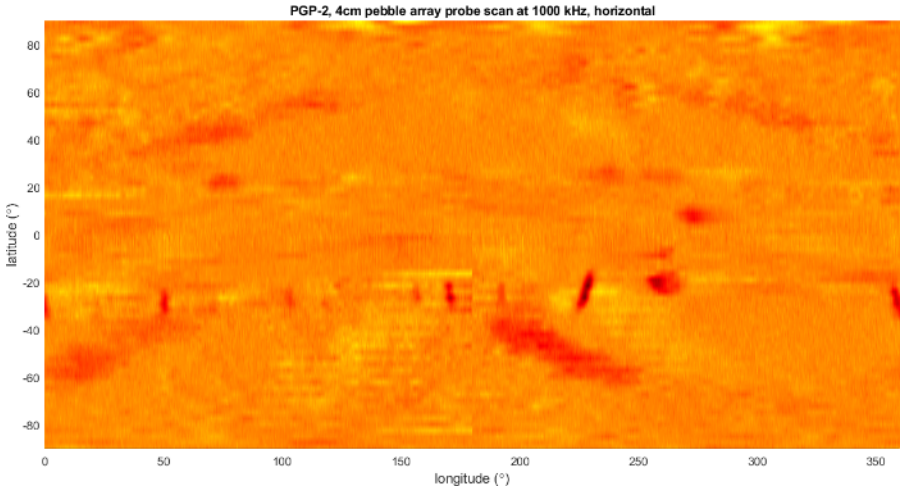

(b)

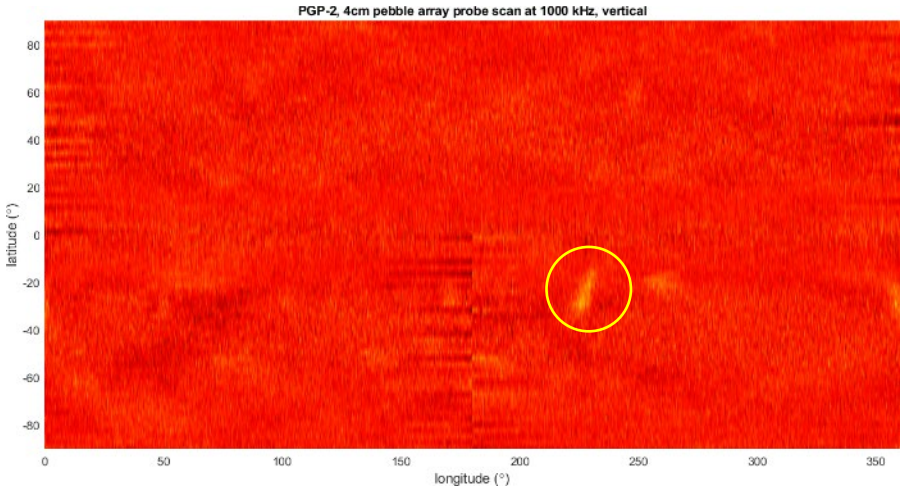

(c)

Figure A-3. PGP-2. Shown here are the eddy current (a) amplitude, (b) horizontal component, and (c) vertical component.

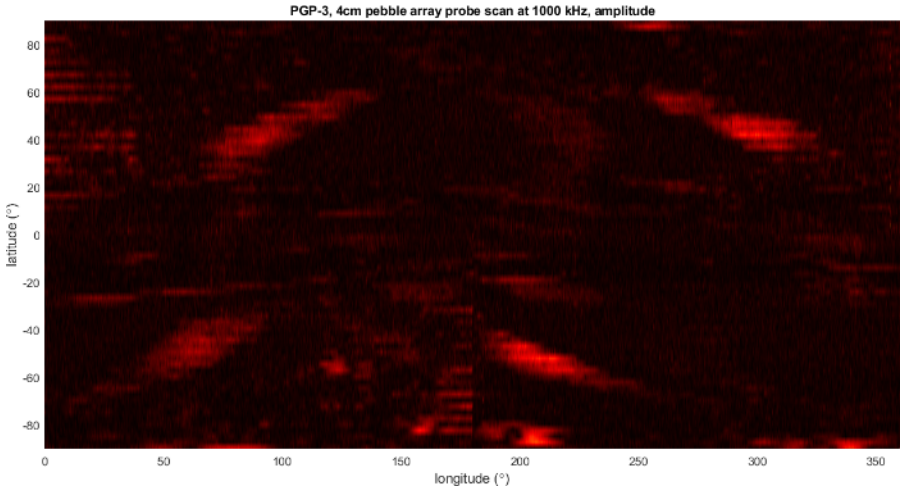

(a)

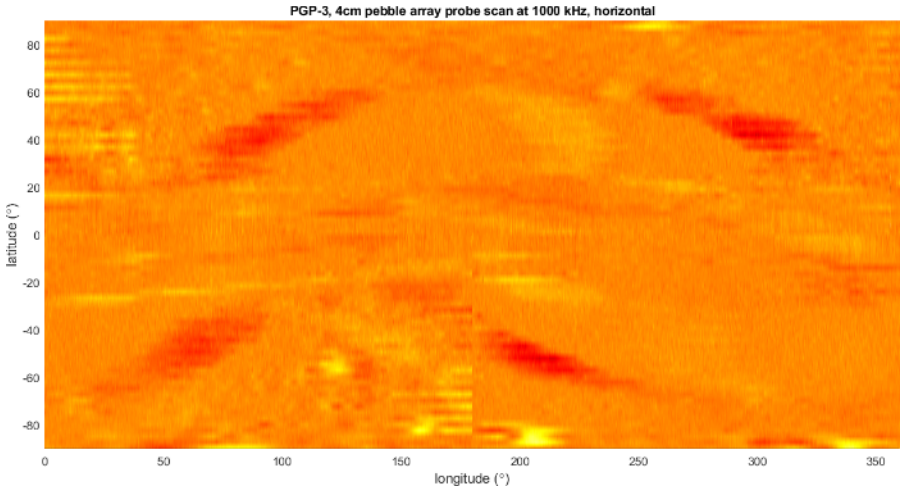

(b)

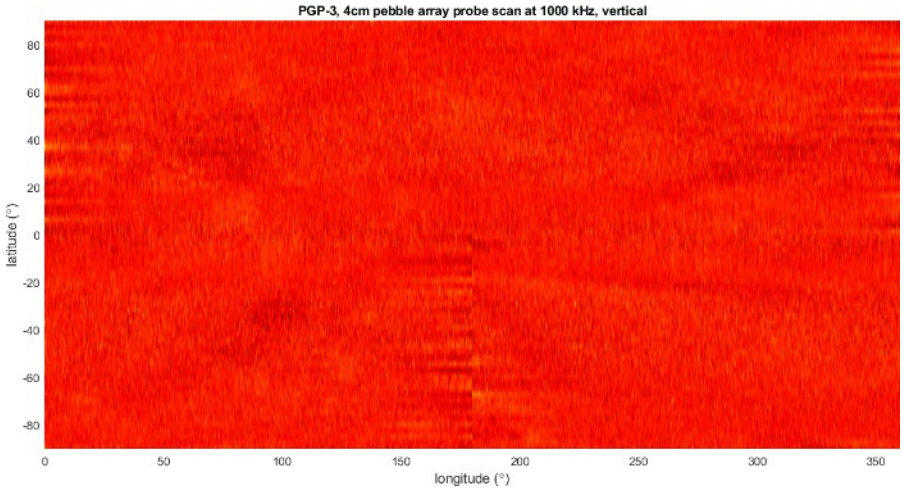

(c)

Figure A-4. PGP-3. Shown here are the eddy current (a) amplitude, (b) horizontal component, and (c) vertical component.

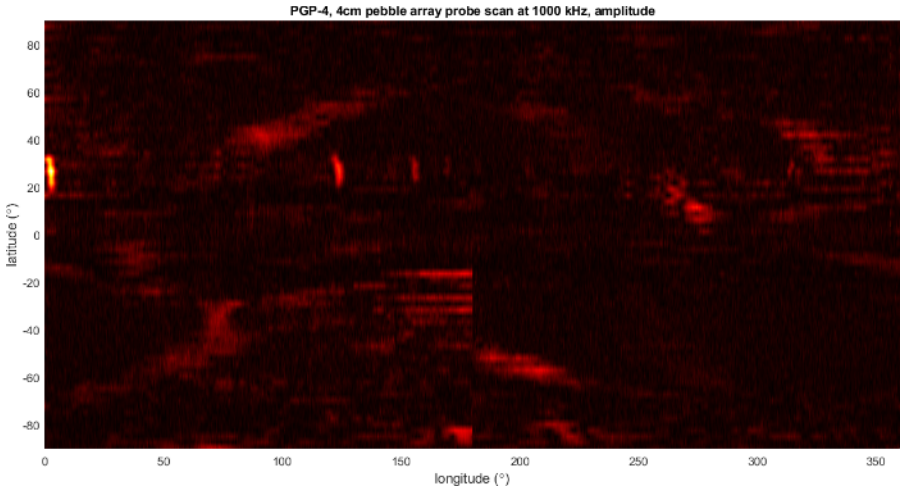
PGP-4, 4cm pebble array probe scan at 1000 kHz, amplitude
latitude (°)
longitude (°)

(a)

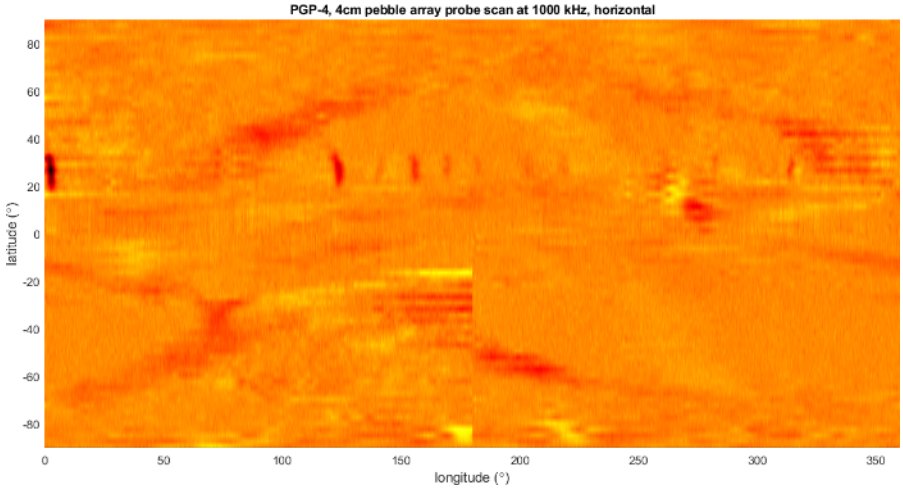
PGP-4, 4cm pebble array probe scan at 1000 kHz, horizontal
latitude (°)
longitude (°)

(b)

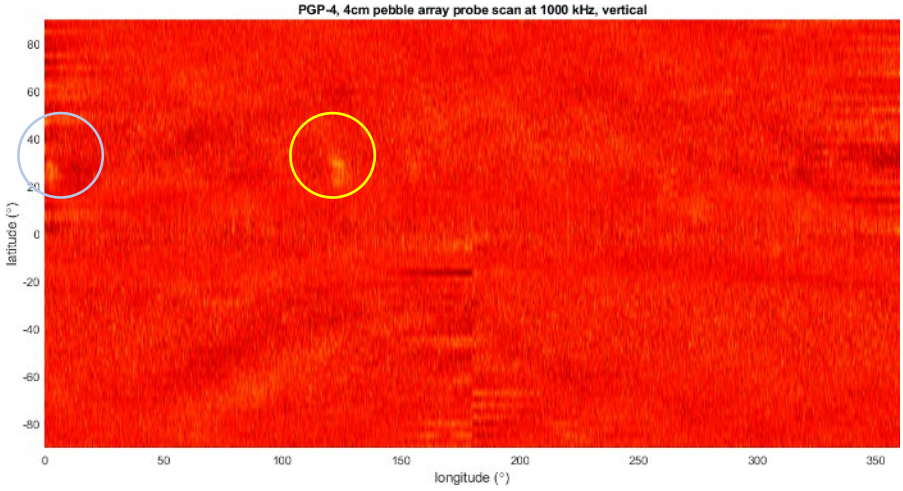
PGP-4, 4cm pebble array probe scan at 1000 kHz, vertical
latitude (°)
longitude (°)

(c)

Figure A-5. PGP-4. Shown here are the eddy current (a) amplitude, (b) horizontal component, and (c) vertical component.

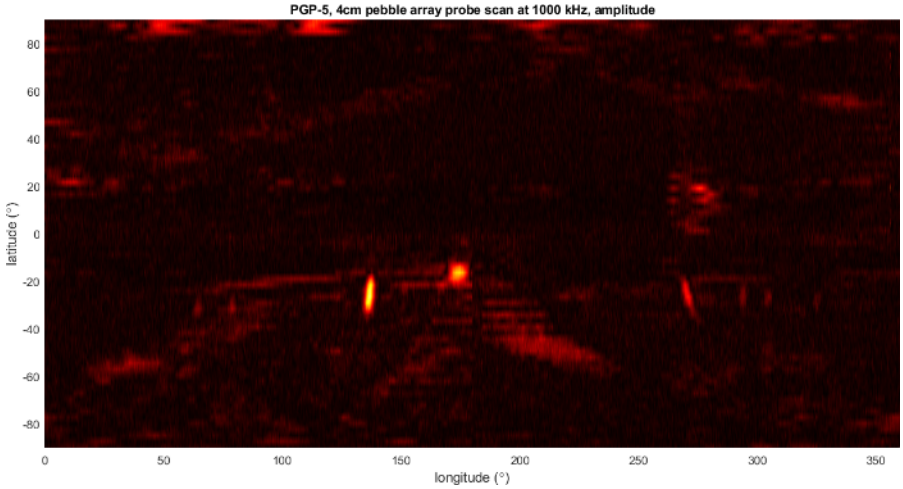

(a)

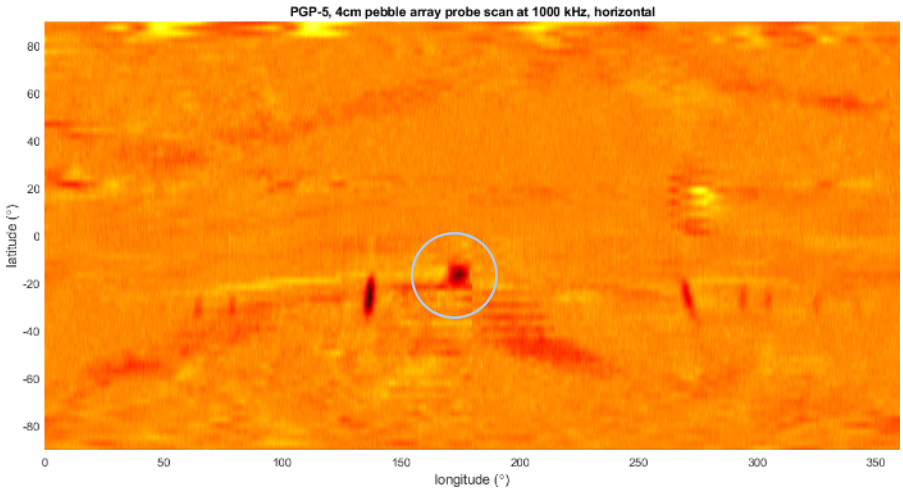

(b)

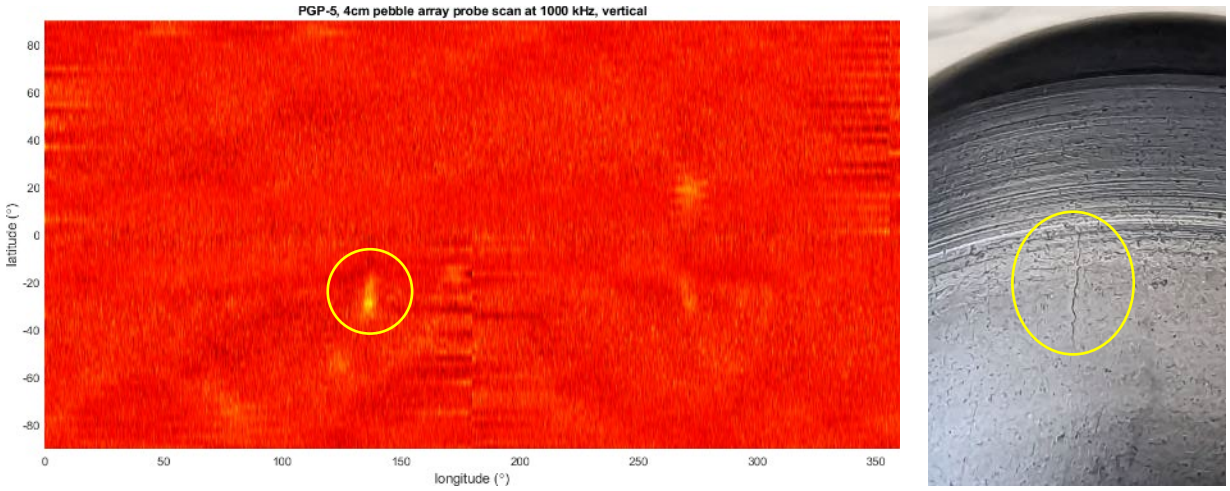

(c)

Figure A-6. PGP-5. Shown here are the eddy current (a) amplitude, (b) horizontal component, and (c) vertical component.

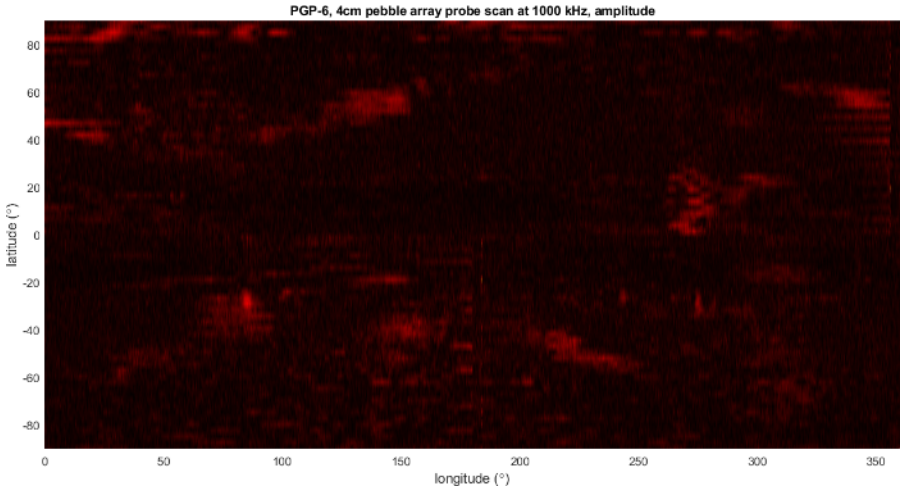

(a)

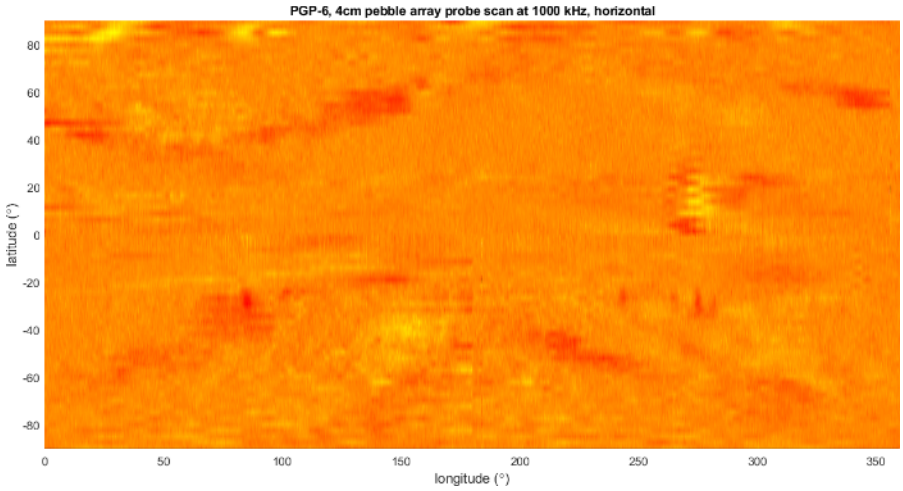

(b)

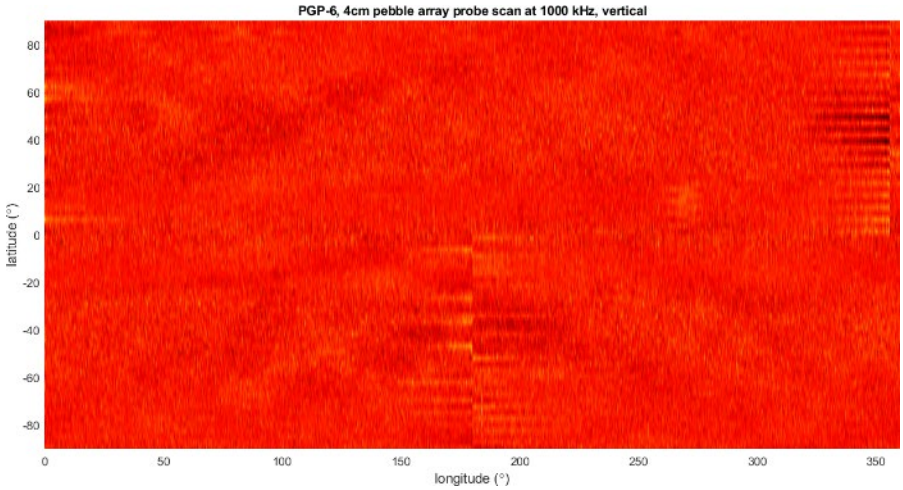

(c)

Figure A-7. PGP-6. Shown here are the eddy current (a) amplitude, (b) horizontal component, and (c) vertical component.

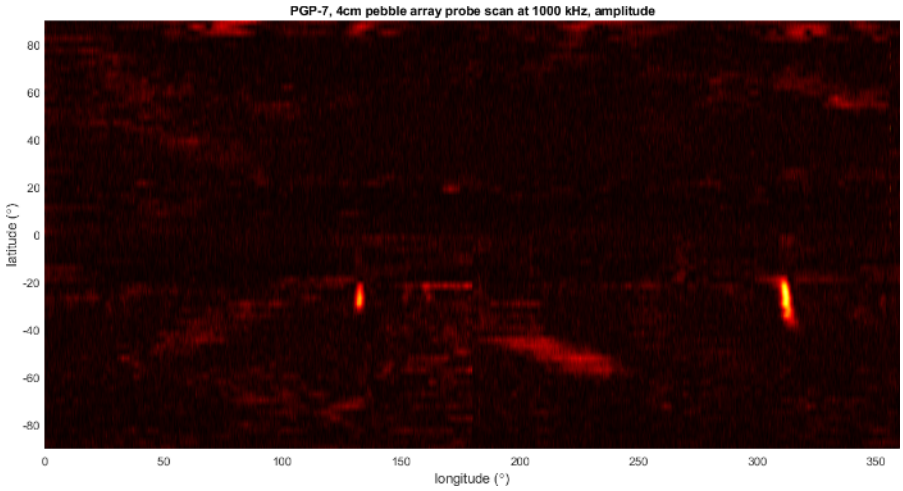
PGP-7, 4cm pebble array probe scan at 1000 kHz, amplitude
latitude (°)
longitude (°)

(a)

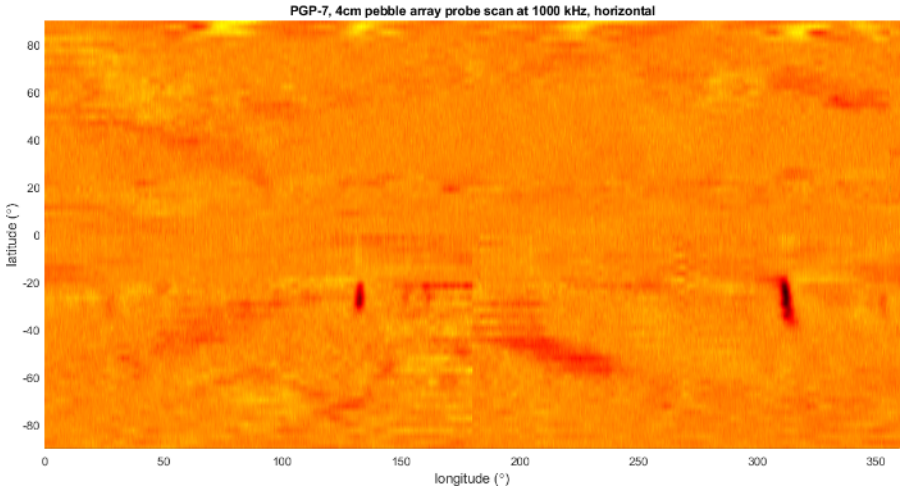
PGP-7, 4cm pebble array probe scan at 1000 kHz, horizontal
latitude (°)
longitude (°)

(b)

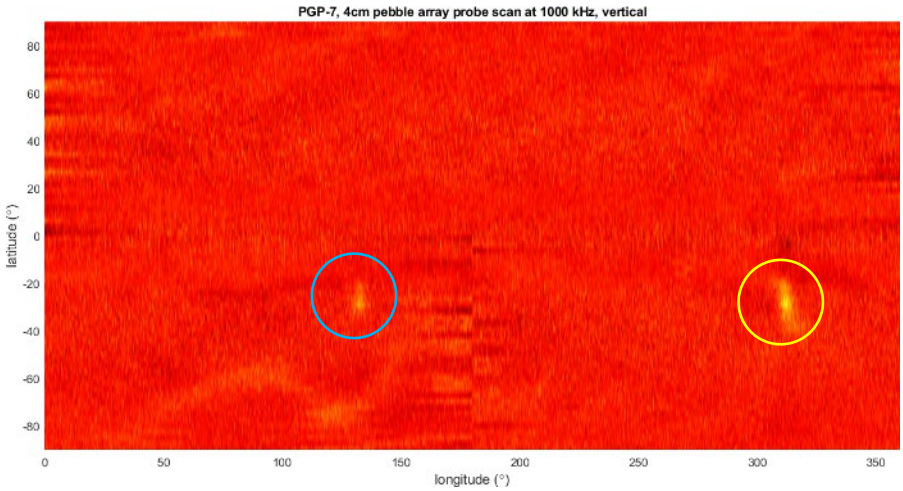
PGP-7, 4cm pebble array probe scan at 1000 kHz, vertical
latitude (°)
longitude (°)

(c)

Figure A-8. PGP-7. Shown here are the eddy current (a) amplitude, (b) horizontal component, and (c) vertical component.

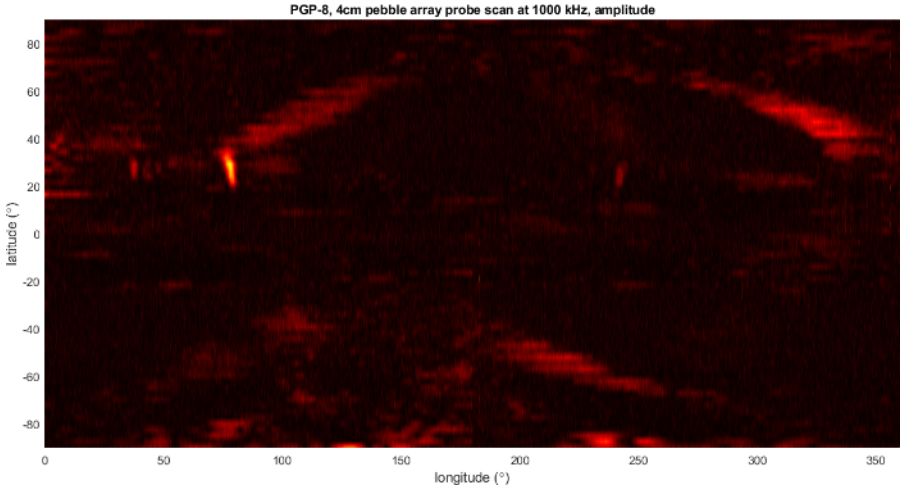

(a)

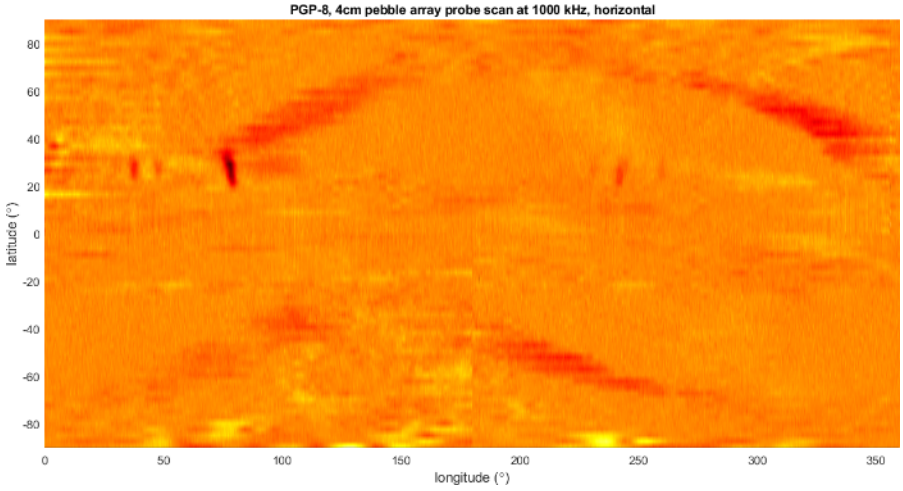

(b)

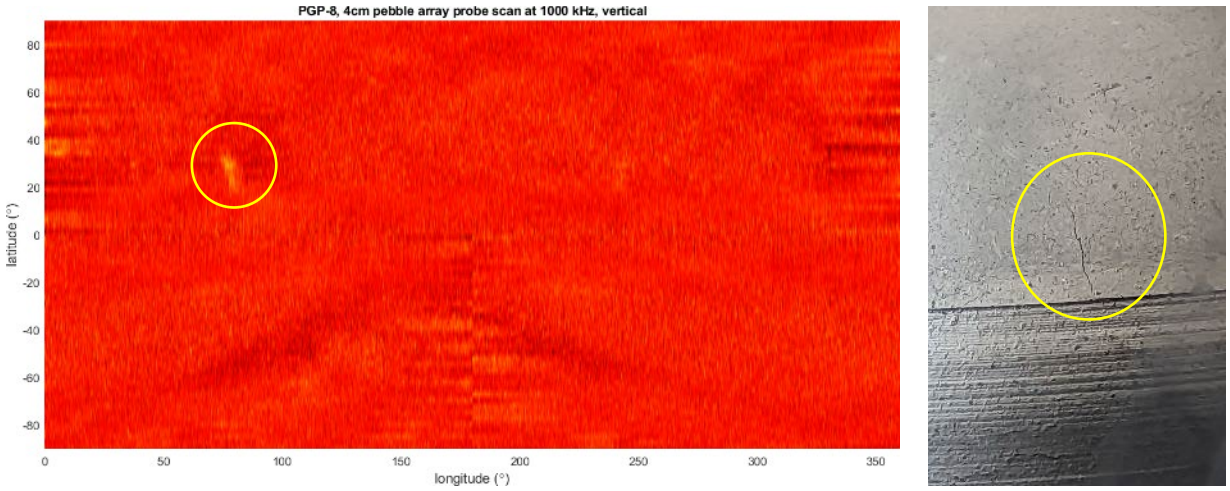

(c)

Figure A-9. PGP-8. Shown here are the eddy current (a) amplitude, (b) horizontal component, and (c) vertical component.

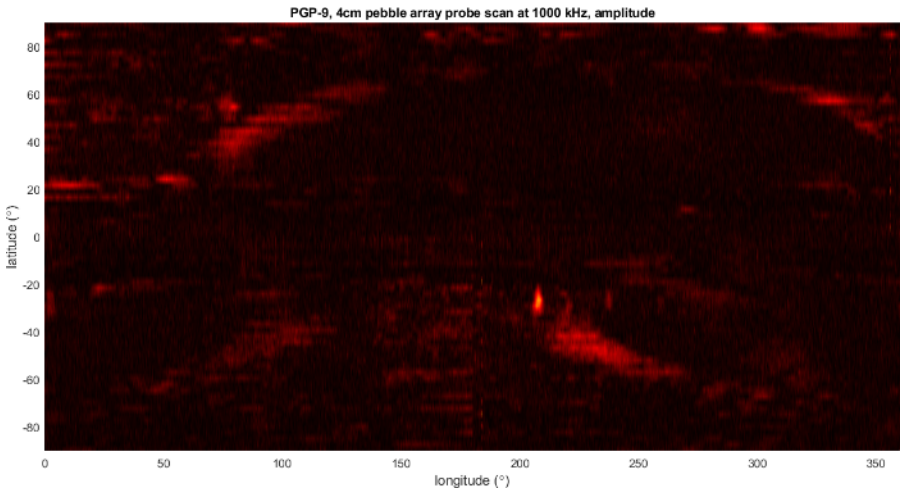

(a)

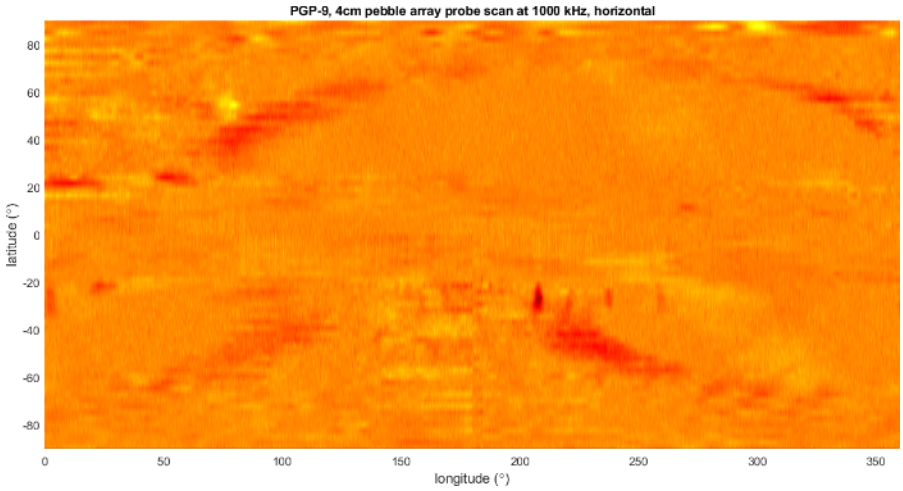

(b)

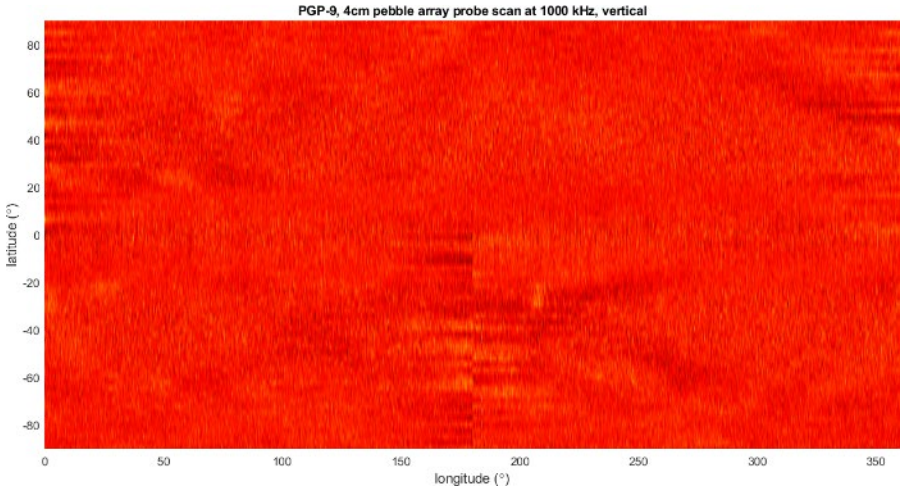

(c)

Figure A-10. PGP-9. Shown here are the eddy current (a) amplitude, (b) horizontal component, and (c) vertical component.